The impact of metal centers in the M-MOF-74 series on carbon dioxide and hydrogen separation

Wasik, Dominika O.; Vicent-Luna, José Manuel; Luna-Triguero, Azahara; Dubbeldam, David; Vlugt, Thijs J.H.; Calero, Sofía

DOI
10.1016/j.seppur.2024.126539

Publication date
2024

Document Version
Final published version

Published in
Separation and Purification Technology

Separation and Purification Technology 339 (2024) 126539

Contents lists available at ScienceDirect

Separation and Purification Technology

journal homepage: www.elsevier.com/locate/seppur

The impact of metal centers in the M-MOF-74 series on carbon dioxide and hydrogen separation

Dominika O. Wasik [a,b], José Manuel Vicent-Luna [a,*], Azahara Luna-Triguero [c,b], David Dubbeldam [d], Thijs J.H. Vlugt [e], Sofía Calero [a,b,**]

[a] Materials Simulation and Modelling, Department of Applied Physics, Eindhoven University of Technology, 5600MB Eindhoven, The Netherlands
[b] Eindhoven Institute for Renewable Energy Systems, Eindhoven University of Technology, PO Box 513, Eindhoven MB 5600, The Netherlands
[c] Energy Technology, Department of Mechanical Engineering, Eindhoven University of Technology, 5600MB Eindhoven, The Netherlands
[d] Van't Hoff Institute for Molecular Sciences, University of Amsterdam, 1098XH Amsterdam, The Netherlands
[e] Engineering Thermodynamics, Process & Energy Department, Faculty of Mechanical Engineering, Delft University of Technology, Leeghwaterstraat 39, Delft 2628CB, The Netherlands

ARTICLE INFO

Keywords:
Monte Carlo
Molecular simulations
Metal-organic frameworks
Adsorption
Force field

ABSTRACT

The series of metal–organic frameworks M-MOF-74 gained popularity in the field of capture and separation of CO_2 due to the presence of numerous, highly reactive open-metal sites. The description of effective interactions between guest molecules and open-metal sites without accounting for polarization effects is challenging but it can significantly reduce the computational cost of simulations. In this study, we propose a non-polarizable force field for CO_2, and H_2 adsorption in M-MOF-74 (M = Ni, Cu, Co, Fe, Mn, Zn) by scaling the Coulombic interactions of M-MOF-74 atoms, and Lennard-Jones interaction potentials between the center of mass of H_2 and the open-metal centers. The presented force field is based on UFF and DREIDING parameters, characterized by high transferability and efficiency. The quantum behavior of H_2 at cryogenic temperatures is considered by incorporating Feynman–Hibbs quantum corrections. To validate the force field, the experimental isotherms of CO_2 at 298 K and 10^{-1} – 10^{2} kPa, the isotherms of H_2 at 77 K and 10^{-5} – 10^{2} kPa, the corresponding enthalpy of adsorption, and the binding geometries in the M-MOF-74 series were reproduced using Monte Carlo simulations in the grand-canonical ensemble. The computed loadings, heats of CO_2 and H_2 adsorption, and binding geometries in M-MOF-74 are in very good agreement with the experimental values. The temperature transferability of the force field from 77 K to 87 K, and 298 K was shown for adsorption of H_2. The validated force field was used to study the adsorption and separation of CO_2/H_2 mixtures at 298 K. The adsorption of H_2 practically does not occur when CO_2 is present in the mixture. As indicated from simulated breakthrough curves, the breakthrough time of CO_2 in M-MOF-74 follows the same order as the uptake and the heat of CO_2 adsorption: Ni > Co > Fe > Mn > Zn > Cu. Increasing the feed mole fraction of CO_2 in the breakthrough simulations from 0.1 to 0.9 speeds up the saturation of the adsorbent, leading to a faster exit of CO_2 with the column effluent. The application of the non-polarizable force field allows full investigation of the capture and separation of CO_2 in M-MOF-74, and can be expanded to study multi-component mixtures or industrial reactions in future research.

1. Introduction

Since metal–organic frameworks (MOFs) emerged in 1995 [1], this class of porous materials has gained attention in a wide variety of applications such as gas storage [2,3], separation [4,5], catalysis [6,7], drug delivery [8,9], enzyme immobilization [10,11], sensing [12,13], and water sustainability [14]. The crystalline structures of MOFs are composed of organic ligands, and metal clusters linked by coordination bonds [15]. The flexibility in modification of physicochemical properties has led to the design of more than 20 000 different MOFs [16]. One of the most popular families of MOFs is M-MOF-74, also known as CPO-27-M, where M = Ni, Cu, Co, Fe, Mn, Mg, or Zn [17–26]. M-MOF-74 series is synthesized by combining M^{2+} ions with 2,5-dioxido-1,4-benzenedicarboxylate ($dobdc^{4-}$) ligands, resulting in hexagonal array of channels, see Fig. 1. Metal ions are favorable sorption sites for

* Corresponding author.
** Corresponding author at: Materials Simulation and Modelling, Department of Applied Physics, Eindhoven University of Technology, 5600MB Eindhoven, The Netherlands.
E-mail addresses: j.vicent.luna@tue.nl (J.M. Vicent-Luna), s.calero@tue.nl (S. Calero).

https://doi.org/10.1016/j.seppur.2024.126539
Received 5 December 2023; Received in revised form 19 January 2024; Accepted 23 January 2024
Available online 1 February 2024

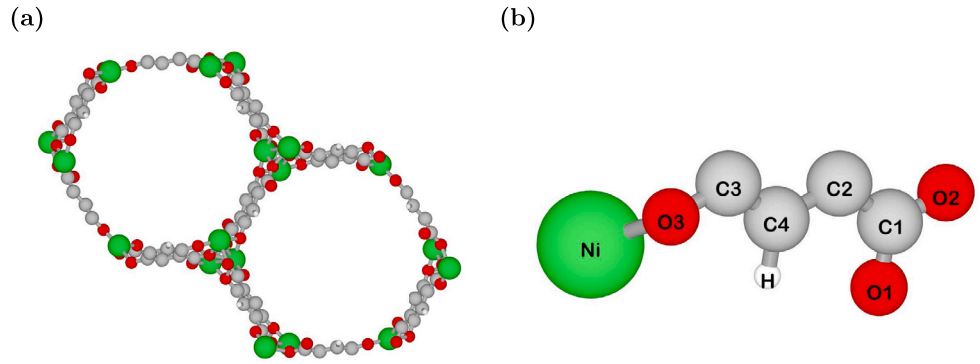

Fig. 1. Schematic representation of M-MOF-74 series on the example of Ni-MOF-74, visualized using iRASPA [33]: (a) an atomistic reference structure of Ni-MOF-74 empty framework, and (b) Ni-MOF-74 building block showing the different uniquely charged atoms. The corresponding charges and LJ interaction potentials are listed in Table S2 of the Supporting Information.

sorbate molecules, accessible through cylindrical pores. Despite the large pores with a diameter of ca. 11 Å [26], the metal cation density is relatively high, due to the negative charge of the dobdc^{4-} ligand [26]. The presence of numerous open-metal sites enhances selectivity [27] and the surface packing density of adsorbates [28], as well as provides reactive sites for chemical reactions, e.g. oxygenation [29], or size-selective Lewis acid catalysis [30]. The stability of metal-ligand complexes for first-row transition metals is described by the empirical Irving–William series [31] and follows the order: $Mn^{2+} < Fe^{2+} < Co^{2+} < Ni^{2+} < Cu^{2+} > Zn^{2+}$. The binding strength between metal cations and ligands, as well as their stability, is related to the lattice constants. The smaller lattice constants correspond to more stable structures and the larger constants to less stable structures [32]. In the study of Yu et al. [32], the experimental lattice constants of M-MOF-74 were compared to the computed from Density Functional Theory (DFT) calculations. The study revealed that the experimental lattice constants *a* and *c* for Mn-, Fe-, Co-, Ni-, and Zn-MOF-74 obey the order of the Irving–William series, as well as the computed lattice constants *a*, however, DFT calculations do not predict this trend correctly for the lattice constants *c* of Fe-, Co-, and Ni-MOF-74.

As effective adsorbents, M-MOF-74 series raised the interest in CO_2 capture, and storage due to alarming fossil CO_2 emissions leading to global warming. Total emissions are estimated at 37.9 Gtons of CO_2 in 2021, with 14% of these emissions from Europe, 13% from the United States, and 33% from China [34]. Liquid absorbent processes are more expensive, and less efficient compared to solid adsorbent processes [35]. In search of an alternative, in the study of Queen et al. [26] the adsorption of CO_2 in M-MOF-74 was analyzed experimentally, and computationally using DFT calculations. The affinity of CO_2 in M-MOF-74, quantified by the isosteric heat of adsorption is in the range from ca. 20 to ca. 40 kJ mol^{-1} [26], resulting in adsorption of CO_2 in M-MOF-74 from ca. 130 mg g^{-1} of framework for M = Cu to as high as ca. 310 mg g^{-1} of framework for M = Mg at 100 kPa, 298 K. Depending on the open-metal site, the isosteric heat of CO_2 adsorption measured at the loading of 0.1 CO_2 per M^{2+} decreases as follows: Mg > Ni > Co > Fe > Mn > Zn > Cu. As the metal-ligand complex stability for the first-row transition metals obeys the Irving–William series order [31]: $Mn^{2+} < Fe^{2+} < Co^{2+} < Ni^{2+} < Cu^{2+} > Zn^{2+}$, ideally the energies of the guest molecule of CO_2 inside the host-MOF and the MOF complexes follow the same trend. The study by Yu et al. [32] revealed that the CO_2 binding strength does not necessarily follow the Irving–William series order, as it is a relative energy to the interaction strength between the CO_2 molecule and the metal centers within the MOF structure: $E_{binding} = E(MOF–CO_2) - E(MOF) - E(CO_2)$. Natural bond order charge analysis showed that the charge transfer from the CO_2 molecule to the metal ions is minimal (0.06–0.07 electron) [32]. This indicates that CO_2 adsorption is predominantly influenced by the electrostatic interactions dependent on the effective charge of the M^{2+} ion at the open-metal site where CO_2 adsorbs. The higher charge on the metal ion leads to the stronger CO_2 binding energy, which correlates with the increased isosteric heat of CO_2 adsorption. The experimental CO_2 binding geometries at different open-metal sites were shown to be in good agreement with DFT computations in the study of Queen et al. [26] The adsorption performance makes the capture and separation of CO_2 from gas mixtures in M-MOF-74 promising [36–40], leading to an idea about the potential application of this MOF series in, e.g., separation of CO_2/H_2 mixtures from the water-gas-shift reaction [41]:

$$CO + H_2O \rightarrow CO_2 + H_2 \quad (1)$$

The presence of CO_2 in H_2 significantly decreases the heat value of produced H_2 as an energy carrier [42]. The separation of H_2 from CO_2/H_2 mixtures is typically performed by pressure swing adsorption (PSA) [43], amine scrubbing [44], and membrane processes [45], although none are commercially used [46]. The improvement of industrial adsorptive H_2 purification efficiency is needed to minimize energy usage in the mass transport of the gas and regeneration of the adsorbents. As further optimization of zeolites and activated carbons is unlikely to result in major enhancements in CO_2/H_2 separation [47], MOFs show promise in this context. In the computational screening study of Aksu et al. [48], the molecular simulation results for zeolites, MOFs, and hypothetical MOFs are compared for syngas separation. The highest CO_2/H_2 selectivity in the range of 24 700–84 000 was reported for MOFs, surpassing zeolites up to ca. 5000 times. In the experimental study of Herm et al. [47], the utility of five MOFs was compared for high-pressure CO_2/H_2 separation by PSA. The highest CO_2/H_2 selectivity in the range of 400–800 at 313 K, 0–40 bar was achieved using Mg-MOF-74, which was chosen as a representative of MOFs with exposed metal cations. The CO_2/H_2 selectivity obtained using Mg-MOF-74 surpassed the performance of the reference activated carbon by ca. 4–8 times. Moreover, the Mg-MOF-74 selectivity exceeded also the representative of MOFs with high surface area and a rigid framework structure, i.e. Be-BTB, by ca. 60–130 times. The observed performance can be associated with interactions involving the open-metal sites, making the M-MOF-74 series an interesting subject for further research. Extensive experimental studies on the adsorption of H_2 using MOFs revealed that the adsorbed H_2 molecules favor the open-metal site over the alternative adsorption site [49]. Due to the open-metal sites present in M-MOF-74 series, H_2 sorption has been studied for M = Ni [17,50,51], Co [19,21,51], Mg [21,51], Zn [22,25,52], Mn [21,51,53], Cu [18,51], and Fe [20,51,54,55]. The two-step mechanism of adsorption, wherein adsorbate molecules first adsorb at the metal centers, followed by adsorption above a triangle of oxygen atoms within the framework, is especially noticeable in the adsorption isotherm and heat of adsorption for Ni-MOF-74 [49]. In the experimental study of Rosnes et al. [51] the uptake of H_2 in M-MOF-74 (M = Ni, Cu, Co, Fe, Mn, Mg)

is determined as ca. 20 mg g^{-1} of framework for M = Ni at 100 kPa, 77 K, and the differences in interactions between H_2 and the metal centers in the structure are examined. A comparison of the isosteric heat of adsorption that quantifies the affinity of H_2, shows the decrease depending on the open-metal site as follows: Ni > Co > Mg > Fe > Zn ≈ Mn > Cu. The difference in affinity compared to CO_2 is attributed to the prevalence of polarization interactions in H_2 sorption, in contrast to electrostatic interactions characterizing CO_2 sorption [23]. Considering that both adsorbates CO_2 and H_2 undergo adsorption in M-MOF-74 with different affinity, an interesting topic for future research is to check, whether the separation of the CO_2/H_2 mixture would be effective.

Apart from the separation of CO_2/H_2 mixtures, another potential application of MOFs is the capture of CO_2 followed by the conversion to useful feedstock chemicals, e.g., formic acid, methanol, urea, propylene, salicylic acid, and polyols [56–59]. The hydrogenation reaction of CO_2 into HCOOH carried out in MOF confinement recently gained interest of scientists [60]. Due to the high kinetic and thermodynamic stability of CO_2 the use of a catalyst is needed to mediate the reduction [61]:

$$CO_2 + H_2 \rightleftarrows HCOOH \quad (2)$$

In our previous study [60], the confinement effect of porous materials on the thermodynamical equilibrium of the CO_2 hydrogenation reaction can be considered as an alternative to high-cost, toxic transition metal catalysts [62]. The performed Monte Carlo simulations of this study proved that the confinement effect of MOFs affects CO_2 hydrogenation reaction, shifting the thermodynamical equilibrium towards HCOOH formation by Le Chatelier's principle [63]. The evaluation of the influence of pore size and metal centers on the HCOOH yield showed that the type of metal center is the prevailing factor. The M-MOF-74 series potentially allows to fully investigate the dependence of HCOOH production enhancement on the type of metal center, minimizing the effect of pore size. Molecular simulations are a natural tool to investigate confinement effects independently from catalytic effects. To the best of our knowledge, there is no literature data regarding force field-based molecular simulations of CO_2/H_2/HCOOH systems in the M-MOF-74 framework. Due to the specific interactions between open-metal sites and polarizable guest molecules, the description of such is challenging. In the studies of Becker et al. [64–66] a polarizable force field for CO_2 in M-MOF-74 was developed. A non-polarizable force field for the adsorption of CO_2 in M-MOF-74 was derived from DFT by Mercado et al. [67,68] by adjusting not only the Lennard-Jones (LJ) interaction potentials of the metal site but all interaction sites. This approach is elaborated and results in many fitting parameters of the force field, possibly leading to lower transferability. An attempt to reproduce experimental data on adsorption of H_2 in M-MOF-74 [51] was made in the study of Pham et al. [23], where the Buch model [69], Belof Stern Space model [70], Darkrim–Levesque model [71], and polarizable Belof Stern Space Polar model [70] of H_2 were tested. Only the polarizable Belof Stern Space Polar model successfully reproduced the experimental adsorption data [51] for all the studied metal centers. Polarizable force fields improve the description of the enhanced interactions between guest molecules and open-metal sites, however, excessive computational costs are generated unless back-polarization is ignored [64]. In the recent study of Becker et al. [66] a polarizable force field for CO_2 in M-MOF-74 is derived directly from quantum mechanics and back-polarization is neglected, resulting in a decrease of the computation time to a level comparable to non-polarizable force fields. In case of systems that include not only CO_2 and H_2 adsorption but also the hydrogenation reaction of CO_2 to HCOOH, the size of the considered system, and the complexity of its description can affect computational time, and accuracy. The development of a non-polarizable force field would be beneficial for further investigation on the dependence of HCOOH production enhancement on the type of metal center in M-MOF-74. Another advantage is the transferability of the non-polarizable force field from one component to another, while polarizable force fields are non-transferable unless they are specifically developed for transferability [23,66]. In this work, we present a non-polarizable force field for molecular simulations of CO_2 and H_2 adsorption in M-MOF-74, where M = Ni, Cu, Co, Fe, Mn, Zn, after introducing two modifications to the existing parameters for CO_2, H_2, and M-MOF-74: (1) Coulombic interactions of M-MOF-74 are scaled to reproduce experimental data on CO_2 adsorption [26] using a non-polarizable force field for CO_2 [72,73] at 298 K, (2) LJ interaction potentials between the center of mass of H_2 in the Darkrim–Levesque model [71], and the open-metal centers are scaled to reproduce experimental data on H_2 adsorption [51] at 77 K. The force field is transferable from cryogenic temperatures (77 K, 87 K) to 298 K, where the separation of CO_2/H_2 mixtures is studied in the M-MOF-74 series. As there is no force field available that would reproduce the adsorption of HCOOH in M-MOF-74, the adjustment of the already existing force field of HCOOH [74] validated in our previous studies [60,75] remains a separated subject of our future research.

Our article is organized as follows: in Section 2, we provide technical details of the molecular simulation methods, the force fields for CO_2, H_2, and the metal–organic frameworks. The force field is adjusted by scaling the Coulombic interaction potentials of M-MOF-74 and scaling the LJ interaction potentials between the center of mass of H_2, and the open-metal centers. The isotherms, and enthalpy of adsorption are computed using Monte Carlo simulations in the grand-canonical ensemble. The force field is validated by reproducing experimental data of CO_2, and H_2 isotherms, enthalpies of adsorption, and binding geometries. The adsorption of CO_2/H_2 mixtures in M-MOF-74 is studied, and the breakthrough curves are generated to analyze the performance of CO_2/H_2 mixtures separation. In Section 3, we present and discuss our results. The non-polarizable force field is able to describe the adsorption behavior and can be applied in computational studies of the capture, and separation processes. Our findings are summarized in Section 4.

2. Methodology

The non-polarizable force field for the adsorption of CO_2 and H_2 in M-MOF-74, where M = Ni, Cu, Co, Fe, Mn, Zn is adjusted, and validated using force field-based molecular simulations. The guest-host and guest-guest intermolecular interactions are modeled by Coulombic and LJ interaction potentials. The Lorentz–Berthelot mixing rules [76] are used to define interactions between unlike Lennard–Jones sites, except for the interactions between the center of mass of H_2 molecules and the open-metal centers, that are scaled and specified by an override. Explicit polarization effects are neglected and accounted for in the LJ and Coulombic interactions. The cutoff radius for intermolecular interactions is set to 12 Å. LJ interactions are cut and shifted to zero at the cutoff without tail corrections. Periodic boundary conditions are exerted in all three directions. The Ewald summation method [77] is used for calculating electrostatic interactions. The Ewald summation method parameters correspond to a relative precision of 10^{-6}. The bond length and the point charges from the model for CO_2 by Harris and Yung [72] are used together with LJ interactions parameters modeled by García-Sánchez et al. [73]. The three-site charge-quadrupole model for H_2 by Darkrim and Levesque [71] was chosen as the closest non-polarizable model to the experimental data studied by Pham et al. [23]. The models of CO_2 and H_2 are rigid. LJ parameters for the atoms of the framework are from the DREIDING force field [78], except for metal centers, which are from the UFF force field [79]. The models of the framework and guest-host interactions used in this work are rigid, and all atoms of the molecules have point charges assigned. All the structures are charge-neutral before and after modification. Each MOF crystal structures for M-MOF-74 were obtained from a different experimental synthesis [17–22]. The parameters of M-MOF-74 trigonal cells are listed in Table S1 of the Supporting Information. The simulated systems are composed of 1 × 1 × 4 unit cells to ensure a minimum distance of more than twice the cutoff radius between periodic images. The LJ parameters, partial

charges for all the components, and frameworks used in this work are listed in Table S2 of the Supporting Information.

The first modification to the existing force field is the scaling of Coulombic interaction potentials of M-MOF-74 to reproduce experimental data on CO_2 adsorption [26]. We implement the RASPA software package [80,81] to perform simulations using the M-MOF-74 frameworks. The adsorption isotherms and the enthalpy of CO_2 adsorption were computed from Monte Carlo simulations in the grand-canonical ensemble (GCMC) [82]. The chemical potential, volume, and temperature are fixed and imposed in the GCMC ensemble. The uncertainties in the computed number of molecules adsorbed in a unit cell were provided by the RASPA software package [80]. The simulation is divided into five blocks, and the error is computed by calculating the standard deviation. The initial charges of the M-MOF-74 frameworks are computed using the 'charge-equilibration' method of Wilmer and Snurr [83,84] at 298 K, and subsequently adjusted through multiplication by a scaling factor within the range of 0.5–1.5. To compare the resulting uptakes and the enthalpies of CO_2 adsorption to the experimental data [26], a series of adsorption isotherms of CO_2 is computed at 298 K, 10^{-1}–10^{2} kPa. The set of charges leading to the closest results to the experimental data was selected for further study as a part of the final force field.

The second modification to the force field is the scaling of LJ interaction potentials between the center of mass of H_2, and the open-metal centers, to reproduce experimental data on the adsorption of H_2 [51]. The LJ interaction potentials were adjusted through multiplication by a scaling factor within the range of 0.8–1.2. However, an exception was made for the potential between the center of mass of H_2 and the open-metal centers in Ni-MOF-74, where a scaling factor of 13 was applied, because of the stronger interaction of H_2 with the metal centers of this MOF [51]. To determine the scaling that leads to the closest values to the experimental loadings and heats of adsorption [51], a series of adsorption isotherms and the enthalpy of H_2 adsorption is computed from GCMC simulations at 77 K, 10^{-5}–10^{2} kPa. Additionally, Henry coefficients computed from the adjusted force field using Widom's test particle insertions [82] at 77 K were compared to the coefficients calculated from the slope of experimental isotherms [51] in the linear region at low pressures [85]. The selected scaling was also validated by simulating the adsorption isotherms of H_2 at 87 K, and 298 K. The quantum behavior that is non-negligible at cryogenic temperatures (i.e. 77 K) was taken into account by incorporating Feynman–Hibbs quantum correction [86] to the interaction potentials between the center of mass of H_2 molecules at 77 K, and 87 K. The influence of Feynman–Hibbs effect on the H_2 adsorption behavior has been already shown to reduce the saturation capacity and change the shape of the isotherms in zeolites and other nanomaterials [87–90]. The original and scaled Coulombic and LJ interaction potentials are provided in Tables 1 and 2, respectively.

The adjusted non-polarizable force field for the adsorption of CO_2, and H_2 in M-MOF-74 was further validated by analysis of the behavior of molecules inside the frameworks at 298 K. To generate binding geometries, Baker's minimization scheme [91] is applied, which uses the eigenvalues/vectors of the Hessian matrix to locate true minima on the energy surface, corresponding to equilibrium geometries. The distance between the metal center and O atom of CO_2 molecule ($M–O_{CO_2}$) was compared with experimental data and DFT [26]. In case of H_2, the simulated distance between the metal center and the center of mass of H_2 ($M–H_{com}$) was compared with DFT [51], as well as the angle between the metal center, the center of mass of H_2, and H atom of H_2 molecule ($M–H_{com}–H_{H_2}$). The CO_2, and H_2 molecules interacting with open-metal centers were visualized using iRASPA [33].

The adjusted, and validated non-polarizable force field was used to study the adsorption of CO_2/H_2 mixtures in M-MOF-74 series. For mole fractions of CO_2: y_{CO_2} = 0.1, 0.5, the adsorption of CO_2, and H_2 was studied at 298.15 K, and 100–4000 kPa, and the results were discussed. The performance of M-MOF-74 in fixed-bed adsorbers was evaluated using breakthrough simulations using the RUPTURA code [92]. The combination of RUPTURA code and the RASPA software enables computation of breakthrough curves directly from GCMC simulations. The computed adsorption data of pure CO_2, and H_2 at 298.15 K, and 100–4000 kPa were used to fit the dual-site Langmuir–Freundlich isotherm model [93], of a functional form:

$$q(p) = \sum_i q_i^{\text{sat}} \frac{b_i (\frac{p_i}{p_0})^{\upsilon_i}}{1 + b_i (\frac{p_i}{p_0})^{\upsilon_i}} \tag{3}$$

where $q(p)$ is absolute loading of the adsorbed phase as a function of pressure, q_i^{sat} is saturation loading, b_i is the coefficient of adsorption representing the affinity of the molecule, υ_i is heterogeneity factor, p_i is the partial pressure in the gas phase in units of Pa, p_0 is the reference pressure equal to 1 Pa, and i refers to component i. The parameters of the dual-site Langmuir–Freundlich model (q_1^{sat}, b_1, υ_1, q_2^{sat}, b_2, and υ_2) for CO_2, and H_2 were used as an input for breakthrough simulations, and are listed in Table S3 of the Supporting Information. The simulations of gas adsorption breakthrough curves were performed for CO_2/H_2 mixtures, where y_{CO_2} = 0.1, 0.2, 0.3, 0.4, 0.5, 0.9, with helium as a carrier gas. To compare the separation of CO_2/H_2 mixtures using M-MOF-74 with performance of modified activated carbon, the initial conditions were selected based on the study of Caldwell et al. [94]: temperature T= 298 K, total pressure p_T = 2.5 MPa, packed bed void fraction ε_B = 0.4, interstitial gas velocity entering the packed bed υ = 0.006791 m s^{-1}, length of packed bed adsorber L = 0.065 m, axial dispersion is neglected, and isothermal conditions are assumed. The output from RUPTURA was validated by independent prediction of CO_2/H_2 mixtures using Ideal Adsorption Solution Theory (IAST) [95], followed by comparison to the previously obtained results from GCMC simulations. The breakthrough curves were analyzed depending on the metal centers, and depending on the mole fraction of CO_2.

The GCMC simulations of the adsorption of CO_2 and H_2 in M-MOF-74 were carried out with 10^4 initialization Monte Carlo (MC) cycles, and $4{\cdot}10^5$ production MC cycles. One single MC cycle includes N MC trial moves, where N is the total number of molecules at the start of the simulation. The probabilities of selecting trial moves in GCMC simulations were 25% translations, 25% rotations, 25% reinsertions, and 25% swap trial moves (exchanging molecules with the reservoir). The GCMC simulations of the CO_2/H_2 mixtures in M-MOF-74 consisted of 10^4 initialization MC cycles, and 10^5 production MC cycles. The probabilities of selecting trial moves were 16.7% translations, 16.7% rotations, 16.7% reinsertions, 16.7% identity changes (changing the identity of the selected molecule) and 33.2% swap trial moves. For more details about Monte Carlo trial moves, the reader is referred to Refs. [33,80,81]

3. Results and discussion

To reproduce experimental data on the adsorption of CO_2 [26], we first computed, and scaled the Coulombic interaction potentials of M-MOF-74, where M = Ni, Cu, Co, Fe, Mn, Zn. The scaled charges are compared to the initial charges computed from the 'charge-equilibration' method in Table 1.

The isotherms and enthalpy of CO_2 adsorption in M-MOF-74 computed with the use of new set of scaled charges at 298 K, and 10^{-1}–10^{2} kPa, are shown in Fig. 2. By only scaling the Coulombic interaction potentials of M-MOF-74 the experimental loadings and heats of adsorption [26] were reproduced, despite starting from isotherms that deviate significantly from the experiment, see an example in Fig. 2c. Overall, the force field agrees well with the experimental measurements, with a small deviation observed for Ni-MOF-74. The highest relative difference of 39% between the computed value of adsorption uptake in Ni-MOF-74 and literature value occurs at 3 kPa. This difference is probably due to the difficulty in describing the two-step mechanism of adsorption in the low-pressure area, wherein adsorbate molecules first adsorb at the

Table 1
The initial charges for M-MOF-74, where M = Ni, Cu, Co, Fe, Mn, Zn computed from the 'charge-equilibration' method of Wilmer and Snurr [83,84], compared to the scaled charges selected based on reproduction of experimental data [26]. The chosen set of charges allows successful computation of the isotherms, and the enthalpy of CO_2 adsorption at 298 K, 10^{-1}–10^{2} kPa. The charges for Co- and Fe-MOF-74 for CO_2 adsorption have been previously published by Luna-Triguero et al. [96].

Atom	Ni-MOF-74		Cu-MOF-74		Co-MOF-74	
	$q_{\text{charge eq.}}/[e^-]$	$q_{\text{scaled}}/[e^-]$	$q_{\text{charge eq.}}/[e^-]$	$q_{\text{scaled}}/[e^-]$	$q_{\text{charge eq.}}/[e^-]$	$q_{\text{scaled}}/[e^-]$
Me	1.10769	1.55	0.923389	0.834	1.16171	1.335
C1	0.431158	0.603	−0.0833878	−0.076	0.422607	0.485
C2	−0.196159	−0.275	0.383558	0.345	−0.179995	−0.207
C3	0.196702	0.275	0.17379	0.156	0.208781	0.245
C4	−0.0609594	−0.086	−0.154189	−0.139	−0.108009	−0.125
O1	−0.449624	−0.63	−0.437776	−0.394	−0.472538	−0.544
O2	−0.581596	−0.815	−0.47853	−0.431	−0.530936	−0.611
O3	−0.50468	−0.702	−0.408696	−0.368	−0.584701	−0.673
H	0.0574637	0.08	0.0818392	0.073	0.0830871	0.095
Atom	Fe-MOF-74		Mn-MOF-74		Zn-MOF-74	
	$q_{\text{charge eq.}}/[e^-]$	$q_{\text{scaled}}/[e^-]$	$q_{\text{charge eq.}}/[e^-]$	$q_{\text{scaled}}/[e^-]$	$q_{\text{charge eq.}}/[e^-]$	$q_{\text{scaled}}/[e^-]$
Me	1.146450	1.226	1.29091	1.161	1.213100	1.006
C1	0.332818	0.356	0.409563	0.368	0.414013	0.343
C2	−0.138145	−0.148	−0.193789	−0.175	−0.186294	−0.155
C3	0.160509	0.175	0.194713	0.175	0.194483	0.161
C4	−0.081881	−0.088	−0.0761898	−0.064	−0.099635	−0.083
O1	−0.562089	−0.602	−0.608495	−0.548	−0.576390	−0.479
O2	−0.410100	−0.439	−0.491698	−0.443	−0.478184	−0.393
O3	−0.523741	−0.561	−0.579225	−0.522	−0.558839	−0.464
H	0.076157	0.081	0.0542353	0.048	0.077740	0.064

Table 2
The initial LJ interaction potentials calculated from Lorentz–Berthelot mixing rules between the center of mass of H_2, and the open-metal centers of M-MOF-74, where M = Ni, Cu, Co, Fe, Mn, Zn, compared to the scaled potentials selected based on reproduction of experimental data [51]. The chosen LJ potentials allow successful computation of the isotherms, and the enthalpy of H_2 adsorption at 77 K, and 10^{-5}–10^{2} kPa.

Metal	$\epsilon/k_{B\,\text{unscaled}}/[K]$	$\epsilon/k_{B\,\text{scaled}}/[K]$	$\sigma_{\text{unscaled}}/[Å]$	$\sigma_{\text{scaled}}/[Å]$
Ni	16.65248	216.4823	2.7415	2.1932
Cu	9.613043	11.5357	3.036	3.036
Co	16.08752	17.6963	2.7585	2.2068
Fe	15.49488	18.5939	2.776	2.776
Mn	15.50317	13.9529	2.798	2.798
Zn	47.85447	43.069	2.7095	2.7095

metal centers, followed by adsorption above a triangle of oxygen atoms within the framework. The tendency in the simulated uptake and heat of CO_2 adsorption agrees with the study by Queen et al. [26]: Ni > Co > Fe > Mn > Zn > Cu. The heats of adsorption for both Co-MOF-74 and Fe-MOF-74 approach ca. 32 kJ mol^{-1} as the uptake reaches 1 CO_2 per M^{2+}, which value is close to the literature data [26], see Fig. 2b. The heat of adsorption for Ni-MOF-74 is found to be somewhat higher, ca. 35 kJ mol^{-1}. This convergence suggests a uniform distribution of adsorption enthalpies at the secondary adsorption sites, reflecting the similarity in adsorption environments across the isostructural series.

The force field has undergone further modifications by the scaling of LJ interaction potentials between the center of mass of H_2, and the open-metal centers to reproduce experimental data on H_2 adsorption [51]. The comparison of the initial LJ interaction potentials from Lorentz–Berthelot mixing rules, and the scaled potentials is shown in Table 2.

The changes in the LJ potential function caused by the scaling and their consequences are shown in Fig. 3 in the example of the adsorption of H_2 in Ni-MOF-74. To reproduce the adsorption isotherm at the low-pressure region, a deeper potential well between the center of mass of H_2 and Ni was necessary, as well as closer intermolecular distance at the energy minimum. This modification allowed the correct reproduction of adsorption at a pressure lower than 10 kPa, which was initially impossible. However, at the range between 10 kPa and 100 kPa the adsorption uptake is overestimated due to the quantum behavior of H_2 molecules at 77 K. This overestimation at cryogenic temperatures was resolved by incorporation of Feynman–Hibbs quantum correction, which affects the shape of the isotherm by reducing the adsorption capacity. The relative difference between the computed value of adsorption uptake using scaled LJ interaction potentials with Feynman–Hibbs quantum correction, and literature value at 100 kPa decreased from 13.3% to 3.6%, leading to the satisfactory reproduction of experimental data.

The isotherms, and the heat of H_2 adsorption computed from the new set of LJ potentials at 77 K, and 10^{-5}–10^{2} kPa are shown in Fig. 4a and b, respectively. The computed isotherms and the heats of adsorption with error bars are presented separately for each studied M-MOF-74 in Figures S1 and S2 of the Supporting Information. While the agreement with the experimental data [51] is satisfactory, larger deviations can be observed for the Co-, and Fe-based frameworks at the low-pressure region, see Fig. 4a. To investigate the agreement of simulated isotherms with the experimental data at the low pressure regime, the Henry coefficients were compared in Table S4 of the Supporting Information. The Henry coefficients for Cu-MOF-74 and Ni-MOF-74 were computed with high accuracy, showing deviations of only 1% and 8%, respectively, when compared to coefficients calculated from experimental adsorption data. The highest deviation from the experimental Henry coefficient value (84%) is observed for Fe-MOF-74. This is reflected in the disparity of the simulated isotherm shape to the experimental data, particularly in the low-pressure region, as shown in Figure S1d of the Supporting Information. The highest relative difference of 60% between the computed value of adsorption uptake and literature value occurs at 0.7 kPa for Fe-MOF-74. The deviation decreases with the increase of pressure to reach a low, acceptable value of 0.7% at 10 kPa. Despite the large discrepancy in the uptake at 0.7 kPa, the corresponding enthalpy of adsorption aligns with the literature value of 8.7 kJ mol^{-1} (the relative difference of 5.8%). It can be observed in Figure S2d of the Supporting Information that the heat of adsorption for Fe-MOF-74 is slightly shifted towards a higher uptake. The shift in a decrease of the computed heat of adsorption indicates that the secondary adsorption sites located directly above a triangle of oxygen atoms within the framework, start filling at ca. 0.8 mol mol^{-1}, 6 kPa, instead of experimental ca. 0.6 mol mol^{-1}, 0.7 kPa. In the simulations, molecules of H_2 and Fe centers are attracting each other too strongly causing higher occupancy of primary adsorption sites than in reality. The trend in the simulated uptake and heat of

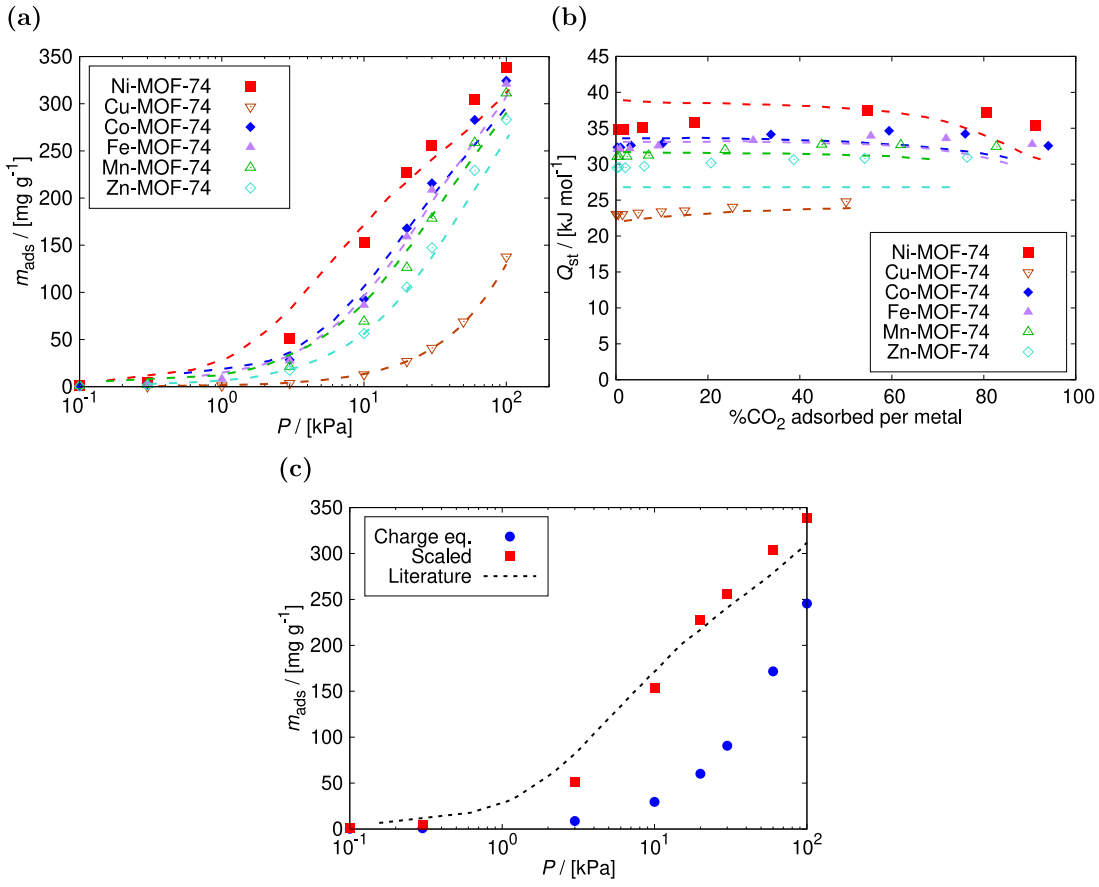

Fig. 2. Adsorption of CO_2 in M-MOF-74 (M = Ni, Cu, Co, Fe, Mn, Zn) computed with the use of new set of scaled charges, that enable the reproduction of experimental data [26] at 298 K, and 10^{-1}–10^{2} kPa: (a) the adsorption isotherms, (b) the heat of adsorption, and (c) the comparison of the experimental adsorption in Ni-MOF-74 [26] to the isotherms computed using the initial charges from the 'charge-equilibration' method, and the new set of scaled charges. Adsorption results computed from modified force field are represented by data points, and the literature data by dashed lines. The force field agrees well with the experimental measurements, and the experimental trend in uptake and heat of CO_2 adsorption is reproduced.

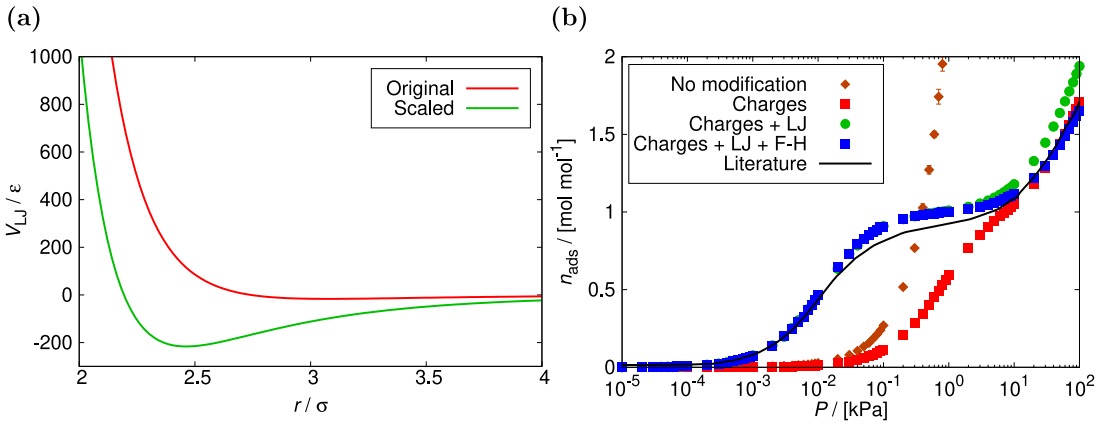

Fig. 3. Adsorption of H_2 in Ni-MOF-74: (a) the original and scaled LJ potential function — intermolecular potential energy as a function of the distance between the center of mass of H_2, and the open-metal center Ni, (b) the comparison of the experimental adsorption isotherm [51] to the isotherms computed from the original force field parameters using the initial charges from the 'charge-equilibration' method, the original force field parameters using the new set of scaled charges, scaled LJ potential between the center of mass of H_2 and Ni using the new set of scaled charges, and scaled LJ potential with Feynman–Hibbs quantum correction using the new set of scaled charges. The simulations were carried out at 77 K, and 10^{-5}–10^{2} kPa. The best agreement with literature data resulted from scaled LJ potential with Feynman–Hibbs quantum correction.

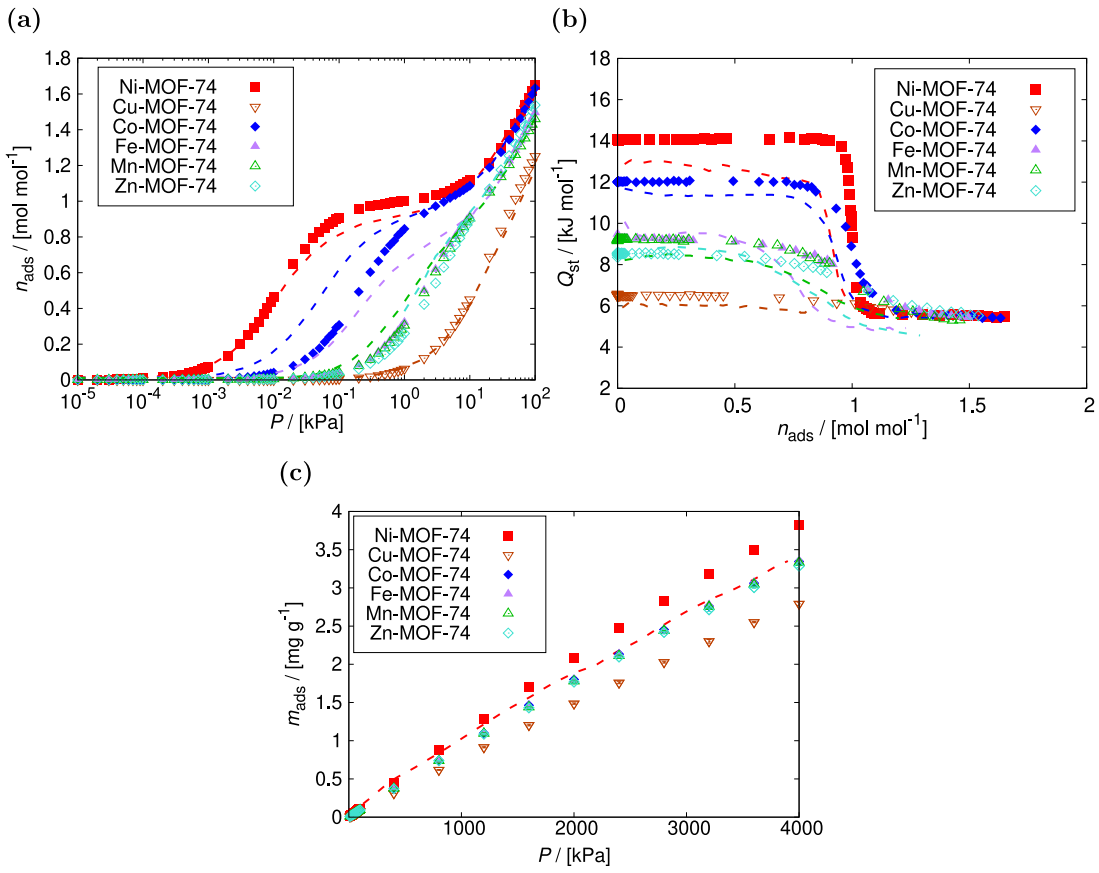

Fig. 4. Adsorption of H_2 in M-MOF-74 (M = Ni, Cu, Co, Fe, Mn, Zn) computed from GCMC simulations with the new set of LJ potentials, that enable the reproduction of experimental data [51]: (a) the adsorption isotherms at 77 K, and 10^{-5}–10^{2} kPa, (b) the heat of adsorption at 77 K, and 10^{-5}–10^{2} kPa, and (c) the adsorption isotherms at 298 K, 10–4000 kPa. Adsorption results computed from modified force field are represented by data points, and the literature data by dashed lines. The force field agrees well with the experimental measurements, with a slight deviation observed for Fe-MOF-74. The experimental trend in uptake and heat of H_2 adsorption is reproduced.

H_2 adsorption agrees with the study by Rosnes et al. [51]: Ni > Co > Fe > Zn ≈ Mn > Cu. The heats of adsorption for all M-MOF-74 frameworks approach ca. 5 kJ mol^{-1} at the secondary adsorption sites, which is in agreement with literature. As in the experiments, the two-step mechanism of adsorption is the most noticeable in case of Ni-MOF-74. The temperature transferability of the force field at cryogenic temperatures was confirmed from 77 K to 87 K, see Figure S4 of the Supporting Information. In Fig. 4c the adsorption of H_2 in M-MOF-74 at 298 K, and 10–4000 kPa were compared to literature data for Ni-MOF-74 [97]. The computed adsorption in Ni-MOF-74 follows the experimental isotherm, but becomes overestimated at 1500 kPa. The relative difference between computed values and literature reaches 14% at 4000 kPa. The trend in the adsorption uptake at 298 K is found to be almost identical as at 77 K: Ni > Co ≈ Fe > Zn ≈ Mn > Cu. We found the performance of the force field to be sufficient at both cryogenic and room temperatures.

The distribution of CO_2, and H_2 molecules can be analyzed inside M-MOF-74 using the average density profiles (Fig. 5). The center of mass of the adsorbed molecules was projected onto the XY plane of anisotropic Ni-, and Cu-MOF-74. The average density profiles of CO_2, and H_2 in Ni-MOF-74 confirm a very high adsorption loading at the open-metal centers compared to the secondary adsorption sites. H_2 molecules are located closer to the metal centers than CO_2, due to their smaller size. The adsorbed molecules of CO_2, and H_2 in Cu-MOF-74 are more homogeneously distributed, especially in case of CO_2. The reason is in the lowest hydrogen affinity for Cu-MOF-74 among the studied structures, and the constant enthalpy resulting in the one-step mechanism of adsorption. The distribution of CO_2, and H_2 molecules inside Co-, Fe-, Mn-, Zn-MOF-74 is shown in Figures S4, and S5 of the Supporting Information, respectively.

The atomistic reference structures of Ni-MOF-74 framework that is loaded with 1.5 CO_2, and 1.5 H_2 per metal site was obtained from Baker's minimization simulations at 298 K. In Fig. 6a, and b the adsorption of CO_2, and H_2 is visualized using iRASPA [33], respectively. The binding geometry of CO_2 molecules resembles the ball-and-stick model from the study of Queen et al. [26], showing a single channel in Fe-MOF-74 loaded with 1.5 CO_2 per Fe center. Two apparent CO_2 sites identified through high resolution neutron powder diffraction experiments exhibit the hexagon-shaped binding pattern, similarly observed here. The pattern is less explicit in case of H_2 but still noticeable at the metal centers.

To examine the binding geometries in more detail, energy minimization simulations using Baker's algorithm were performed for a single molecule of the adsorbate at 298 K. The computed distances M–O_{CO_2}, and M–H_{com}, along with the angles M–H_{com}–H_{H_2} are compared with literature data [26,28,51,53,55,98] in Table 3.

The computed binding geometries are in a very good agreement with the reference values. The relative difference between the computed and experimental M–O_{CO_2} distances is 3%–7%. Similarly, in the case of M–H_{com} the relative difference is 0.3%–10%. Surprisingly, the closest result to the literature data (0.3%) was achieved for Fe-MOF-74, whose computed adsorption isotherm deviated the most from the experimental. The highest relative difference of 10.3% is between the computed and experimental Cu–H_{com} distance. In addition to neutron diffraction, Rosnes et al. [51] performed DFT computations at the PBE + D level resulting in Cu–H_{H_2} distances of 2.75 Å, and 2.66 Å that are close to our values: 2.744 Å, and 2.743 Å (the relative difference of 2.4% and 0.2%, respectively). The computed angles M–H_{com}–H_{H_2} for Co-, and Ni-MOF-74 agree with the results from DFT reported by Pham

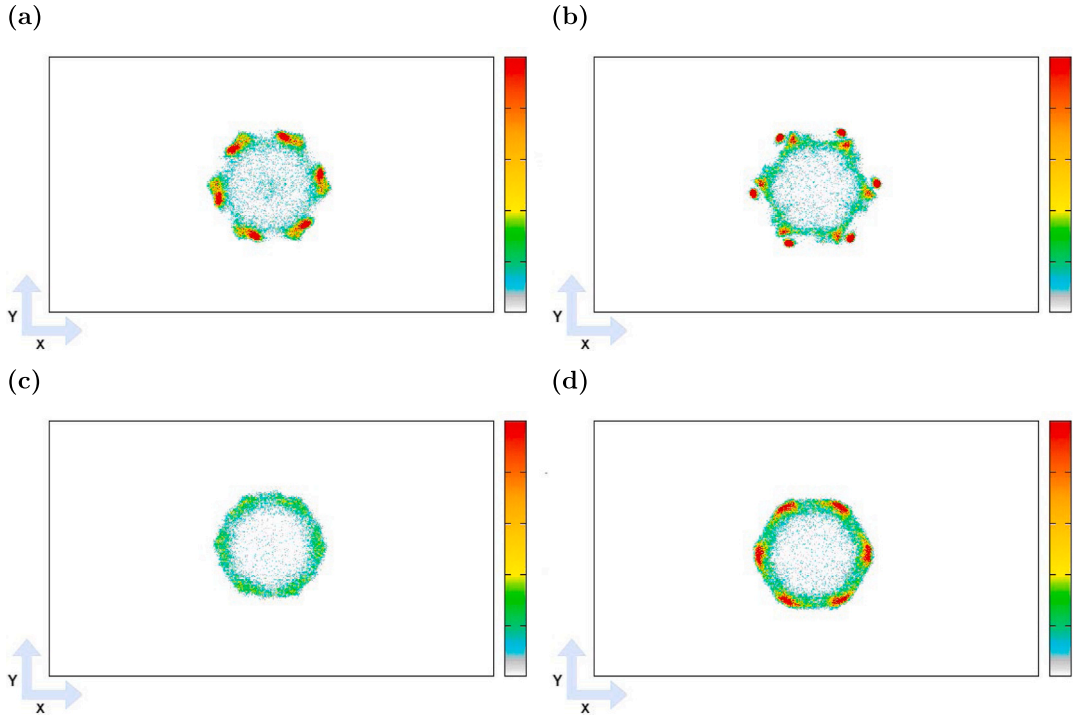

Fig. 5. The distribution of the CO_2, and H_2 molecules inside M-MOF-74, analyzed using density profiles from GCMC simulation: (a) the distribution of CO_2 molecules in Ni-MOF-74 at 298 K, 100 kPa, (b) the distribution of H_2 molecules in Ni-MOF-74 at 77 K, 100 kPa, (c) the distribution of CO_2 molecules in Cu-MOF-74 at 298 K, 100 kPa, (d) the distribution of H_2 molecules in Cu-MOF-74 at 77 K, 100 kPa. The center of mass of the molecules that are adsorbed was projected onto the XY plane. The color gradation of the scales relates to the most and least populated regions of the structure, which is relative in each case. The color scale is shown as a reference of the molecules loading. The preferential sites of CO_2, and H_2 molecules (colored red) in Ni-MOF-74 are at the open-metal centers. The adsorption loading of CO_2, and H_2 in Cu-MOF-74 is more homogeneously distributed, which is a reflection of the lower hydrogen affinity for Cu.

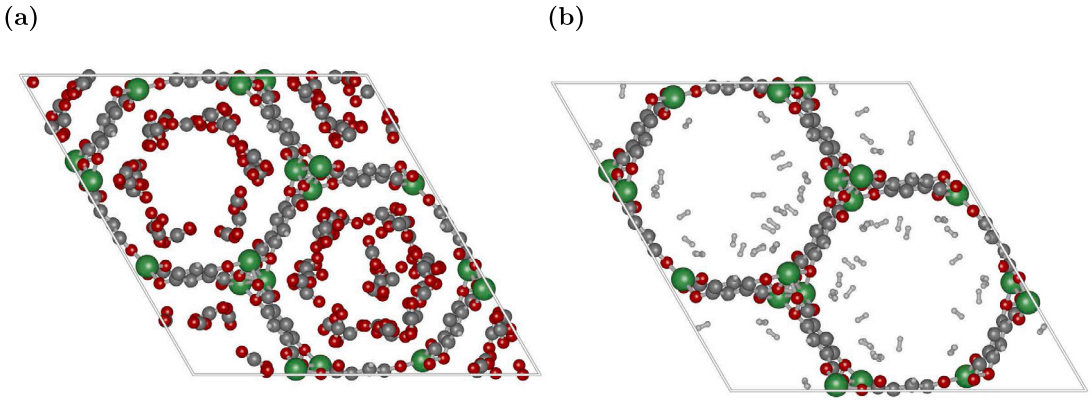

Fig. 6. The atomistic reference structures of Ni-MOF-74 framework obtained from Baker's minimization simulations at 298 K: (a) loaded with 1.5 CO_2 per metal site, and (b) loaded with 1.5 H_2 per metal site. The hexagon-shaped binding pattern of adsorbate molecules shown in the study of Queen et al. [26] is also displayed here, especially for CO_2 molecules. The molecules of H_2 are located mostly at the metal centers.

Table 3
Binding geometry of CO_2, and H_2 molecules in M-MOF-74 obtained from Baker's minimization simulations at 298 K. The computed distances M–O_{CO_2}, and M–H_{com}, together with the angles M–H_{com}–H_{H_2} are compared to the literature data [26,28,51,53,55,98]. The computed binding distances are in a very good agreement with the reference values. The relative differences between our results and experimental studies are lower than 10%. The binding distances and angles are visualized in Fig. 7.

Metal	M–$O_{CO_2,exp}$ [26] [Å]	M–$O_{CO_2,DFT}$ [26] [Å]	M–$O_{CO_2,sim}$ [Å]	M–$H_{com,exp}$ [Å]	M–$H_{com,sim}$ [Å]	M–H_{com}–$H_{H_2,sim}$ [°]
Ni	2.29[98]	2.52	2.39	2.20[53]	2.329	88.675
Cu	2.86	2.87	2.69	3.03[51]	2.718	89.93
Co	2.26	2.56	2.42	2.23[53]	2.159	89.189
Fe	2.29	2.62	2.43	2.53[55]	2.522	89.057
Mn	2.51	2.57	2.44	2.67[51]	2.524	87.932
Zn	2.43	2.84	2.57	2.6[28]	2.637	89.933

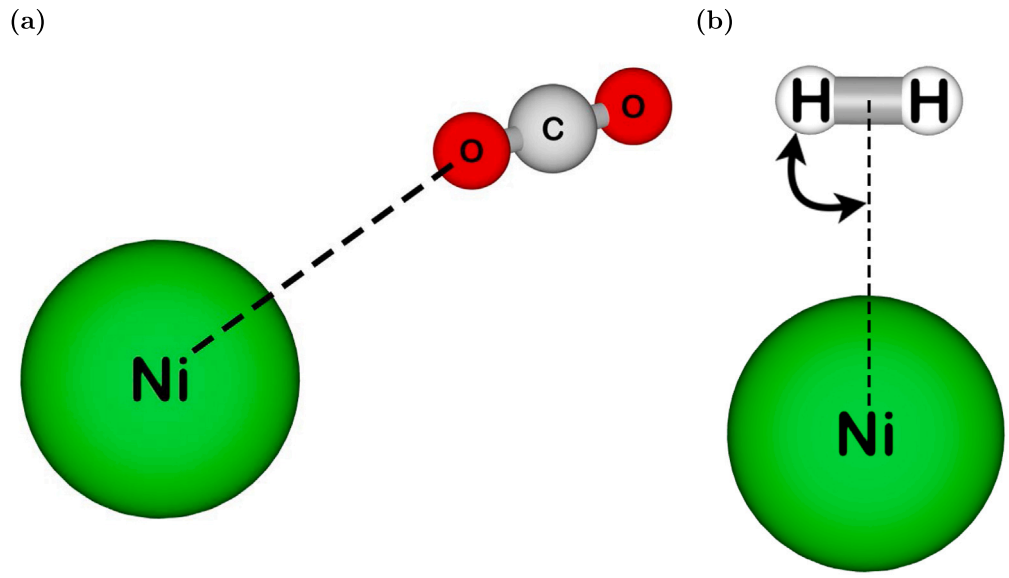

Fig. 7. Binding geometry of the adsorbate molecule in Ni-MOF-74 obtained from Baker's minimization simulations at 298 K: (a) CO_2, and (b) H_2. The molecules interacting with open-metal centers are visualized using iRASPA [33]. The binding distances subject to analysis in Table 3 ($M–O_{CO_2}$, and $M–H_{com}$) are connected by dashed lines. The angle $M–H_{com}–H_{H_2}$ is depicted by an arc.

et al. [23] (83.7° and 76.9°, respectively) with the deviation of 7% and 15%, although in the case of Zn (60.8°) almost 50% of relative difference is observed. The CO_2, and H_2 molecules interacting with open-metal centers of Ni-MOF-74 are visualized using iRASPA [33] in Fig. 7.

The non-polarizable force field for adsorption of CO_2, and H_2 in M-MOF-74 has been validated by reproducing the experimental data of adsorption isotherms, the heats of adsorption and binding geometries, and therefore used to predict the adsorption of CO_2/H_2 mixture. The adsorption of CO_2/H_2 mixture in M-MOF-74 at 298.15 K, and 100–4000 kPa is shown for CO_2 mole fraction y_{CO_2} = 0.1 in Fig. 8a, and y_{CO_2} = 0.5 in Fig. 8b. When CO_2 is present in the gas mixture even at the lowest studied mole fraction y_{CO_2} = 0.1, the adsorption of H_2 practically does not occur (it is lower than 1 mg g^{-1} of H_2). This is due to much higher CO_2 affinity for M-MOF-74 of ca. 30 kJ mol^{-1} at the secondary adsorption sites than the affinity of H_2 (ca. 6 kJ mol^{-1}). The adsorption loading decreases with mole fraction of CO_2. Compared to the adsorption of pure CO_2, its uptake from CO_2/H_2 mixture in Ni-MOF-74 at 100 kPa decreased by 1.2 times for y_{CO_2} = 0.5, and by 2.3 times for y_{CO_2} = 0.1. Similarly, the saturation loading for y_{CO_2} = 0.1 decreased by 1.2 times compared to y_{CO_2} = 0.5. The tendency in performance of M-MOF-74 has changed slightly for mixture with y_{CO_2} = 0.5, compared to the tendency in adsorption of pure CO_2 (Ni > Co > Fe > Mn > Zn > Cu): the adsorption uptakes in Co-, Fe-, and Mn-MOF-74 surpassed the results in Ni-MOF-74 at high pressure. In case of Co-, Mn-, and Ni-MOF-74 the adsorption loadings overlap within the error bars. The adsorption in Fe-MOF-74 is likely overestimated, due to small discrepancies between the model and the experimental adsorption isotherm of H_2 described earlier in this manuscript, that might affect the adsorption of CO_2. The mole fraction of CO_2 in the gas mixture also affects the shape of Cu-MOF-74 isotherm. The increase in mole fraction of CO_2 causes saturation to be achieved in Cu-MOF-74 at lower pressure (ca. 2000 kPa), while in case of lower mole fraction of CO_2 the loading is still growing.

In Fig. 9, the distributions of the CO_2 and H_2 molecules adsorbed from CO_2/H_2 gas mixture with CO_2 mole fraction y_{CO_2} = 0.5 are analyzed inside Ni- and Cu-MOF-74 at 298.15 K and 4000 kPa. The preferential sites of the CO_2 molecules adsorbed in Ni- and Cu-MOF-74 are located at the open-metal centers and in the middle of the pores. The adsorption loading of H_2 in Ni- and Cu-MOF-74 is homogeneously distributed, which reflects the lower hydrogen affinity compared to CO_2, resulting in the adsorption uptake lower than 1 mg g^{-1} of H_2.

The process of CO_2 separation from CO_2/H_2 mixtures using M-MOF-74 is promising as the molecules of H_2 do not adsorb, resulting in high purity products. The performance of M-MOF-74 was further evaluated in fixed-bed adsorbers using breakthrough simulations from RUPTURA. The breakthrough curves were computed for CO_2/H_2 mixtures, where CO_2 mole fraction y_{CO_2} = 0.1, 0.2, 0.3, 0.4, 0.5, 0.9, see Fig. 10. The validation of output from RUPTURA by independent prediction of CO_2/H_2 mixtures from Fig. 8 using IAST is shown in Figure S6 of the Supporting Information. The prediction obtained using IAST from RUPTURA agrees well with the previously performed GCMC simulations of the CO_2/H_2 mixture, indicating the successful validation of results from RUPTURA. It is clear that the separation of CO_2 is effective, as H_2 is not being adsorbed from the gas mixture. The analysis of breakthrough curves of CO_2 obtained in Ni-, and Cu-MOF-74 (Fig. 10a, and b) shows that the breakthrough time increases with decreasing mole fraction of CO_2 in the mixture. More adsorbate molecules flowing through a column result in faster filling of the adsorbent. Increasing the feed mole fraction of CO_2 from 0.1 to 0.9 speeds up the breakthrough time by ca. 40 min in Ni-MOF-74, and ca. 16 min in Cu-MOF-74. CO_2 eluted out up to 2 times later in case of Ni-MOF-74 than Cu-MOF-74. The adsorption uptake in Ni-MOF-74 is significantly higher than in Cu-MOF-74, consequently the maximum loading of column containing Ni-MOF-74 takes longer under the same conditions. The tendency in performance of all the studied M-MOF-74 is indicated in Fig. 10c for the mixture with y_{CO_2} = 0.5. The time needed for CO_2 to elute out follows the same order as the uptake and the heat of CO_2 adsorption: Ni > Co > Fe > Mn > Zn > Cu, with the time difference of ca. 3 min between Ni-, and Cu-MOF-74. The breakthrough curves for Co-, Fe-, Mn-, and Zn-MOF-74, where CO_2 mole fraction in the mixture is y_{CO_2} = 0.1, 0.2, 0.3, 0.4, 0.5, 0.9 are shown in Figure S7 of the Supporting Information. The comparison of breakthrough curves depending on the metal centers for mixtures with y_{CO_2} = 0.1, 0.9 is shown in Figure S8 of the Supporting Information. The breakthrough time difference between Ni-, and Cu-MOF-74 is shown to decrease with increasing feed mole fraction of CO_2. At y_{CO_2} = 0.1 the breakthrough time difference is 24 times longer than at y_{CO_2} = 0.9. In the study of Caldwell et al. [94] the separation of CO_2/H_2 mixtures was performed using modified activated carbon at y_{CO_2} = 0.1, 0.2, 0.3, 0.4, 0.5, at the same initial

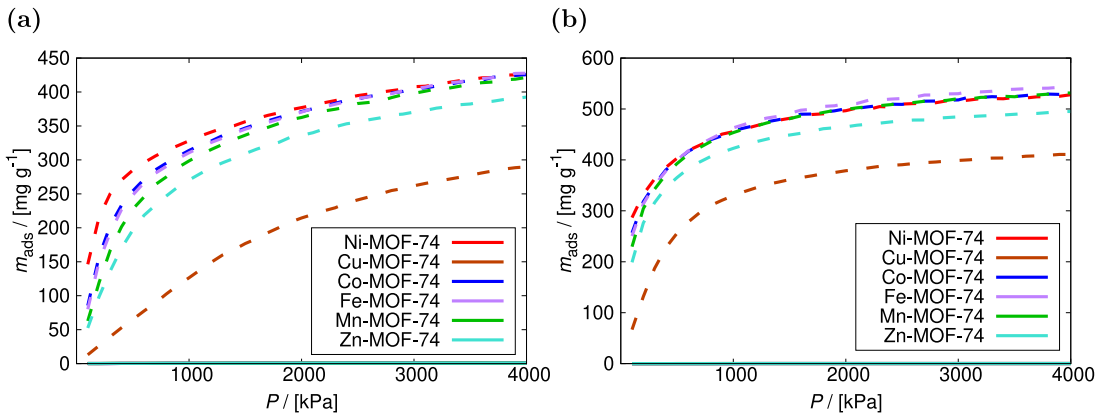

Fig. 8. Adsorption of CO_2/H_2 mixture in M-MOF-74 obtained from GCMC simulations at 298.15 K, and 100–4000 kPa for CO_2 mole fraction: (a) y_{CO_2} = 0.1, and (b) y_{CO_2} = 0.5. The adsorption isotherms of CO_2 are represented by dashed lines, and the adsorption isotherms of H_2 by solid lines. The adsorption of H_2 practically does not occur when CO_2 is present in the mixture. The adsorption loading in all studied M-MOF-74 decreases with mole fraction of CO_2.

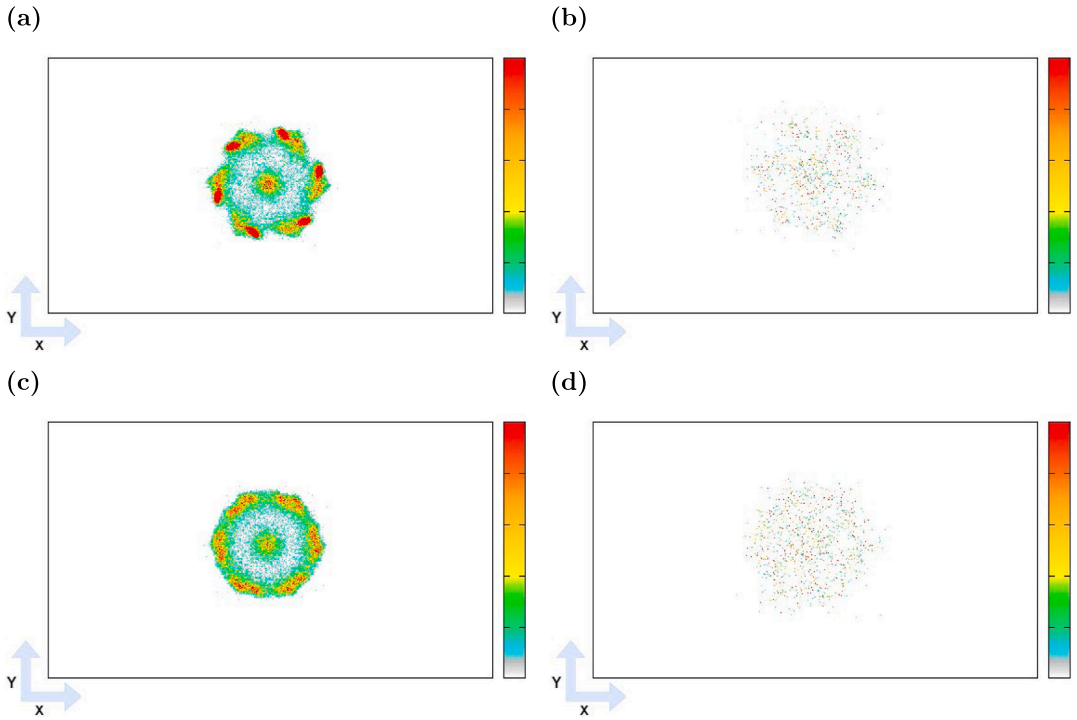

Fig. 9. The distribution of the CO_2, and H_2 molecules inside M-MOF-74, analyzed using density profiles from GCMC simulations of CO_2/H_2 gas mixture (y_{CO_2} = 0.5) at 298.15 K, 4000 kPa: (a) the distribution of CO_2 molecules in Ni-MOF-74, (b) the distribution of H_2 molecules in Ni-MOF-74, (c) the distribution of CO_2 molecules in Cu-MOF-74, (d) the distribution of H_2 molecules in Cu-MOF-74. The center of mass of the molecules that are adsorbed was projected onto the XY plane. The color gradation of the scales relates to the most and least populated regions of the structure, which is relative in each case. The color scale is shown as a reference of the molecules loading. The preferential sites of CO_2 molecules (colored red) in Ni- and Cu-MOF-74 are at the open-metal centers and in the middle of the pores. The adsorption loading of H_2 in Ni- and Cu-MOF-74 is homogeneously distributed, which is a reflection of the lower hydrogen affinity compared to CO_2, resulting in the adsorption uptake lower than 1 mg g^{-1} of H_2.

conditions as specified in this study. The recorded breakthrough time was between ca. 17 min for y_{CO_2} = 0.5, and ca. 50 min for y_{CO_2} = 0.1. This is a very similar time difference as Ni-MOF-74, in which case the breakthrough time equals to ca. 12 min for y_{CO_2} = 0.5, and ca. 45 min for y_{CO_2} = 0.1. The CO_2/H_2 separation performance of Ni-MOF-74 is found to be comparable to the modified activated carbon. We feel that other factors important for Ni-MOF-74 application in PSA, such as economic analysis, resistance to moisture, and structural modifications, are beyond the scope of the present study. As MOF crystals are brittle and easily broken [99], their application in powder form leads to a high-pressure drop across the column and dust pollution. For scalable industrial applications, Ni-MOF-74 should be pressed into the pellets [100], or molded into processable shaped bodies of high porosity [101]. The molding process was described in the study of Pu et al. [101] based on Mg-MOF-74. The authors showed that the molding process rarely reduces the adsorptive ability. Another interesting topic explored in the literature involves modifications of M-MOF-74: the development of zeolite@metal–organic framework composites consisting of Ni-MOF-74 and zeolite-5 A with a core–shell structure for efficient H_2 purification [102]. Al-Naddaf et al. [102] reported that the selectivities for separations of CO_2/H_2, CO/H_2, CH_4/H_2, and N_2/H_2 are larger than those of the bare zeolite or MOF. Due to a higher surface area, total pore volume, and formation of new mesopores at the MOF–zeolite interface, the composite showed a 20%–30% increase in CO_2, CO, CH_4, and N_2 uptake than Ni-MOF-74 [102]. An alternative, worth exploring post-modification of Ni-MOF-74 is also amino-functionalization with

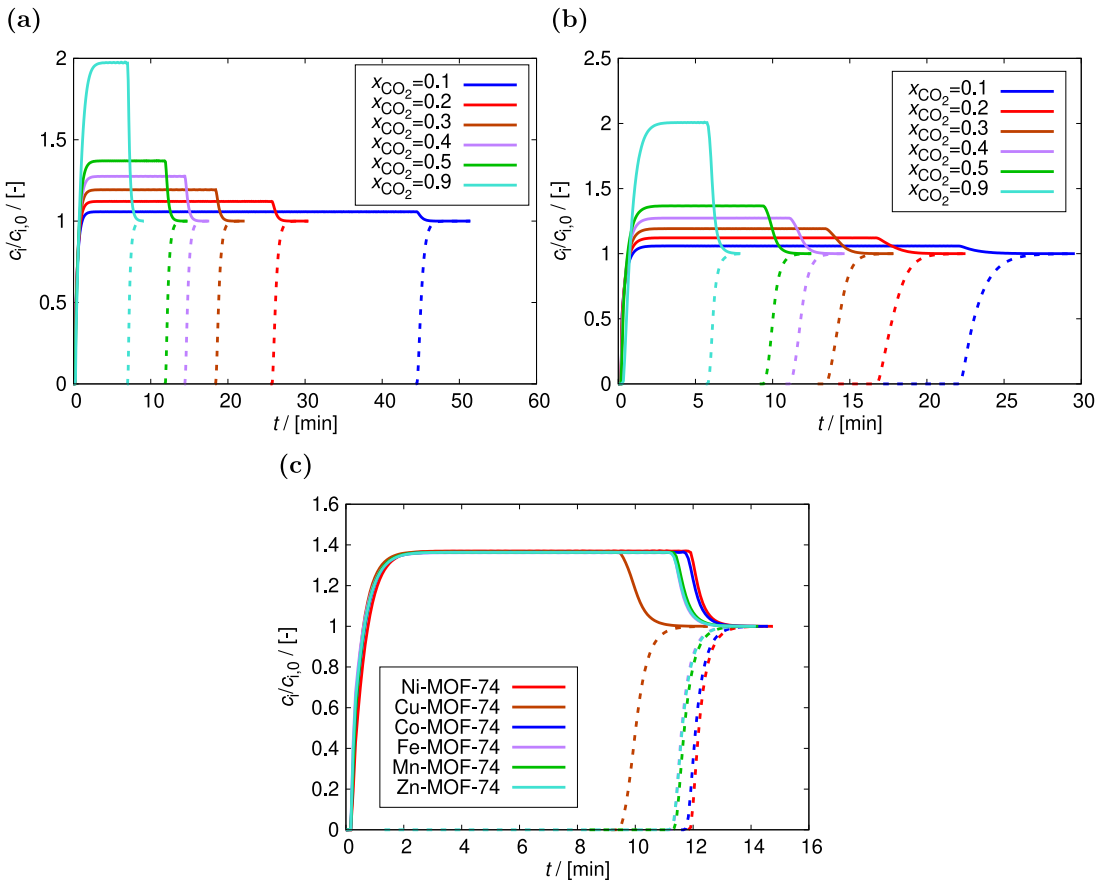

Fig. 10. Breakthrough curves computed from RUPTURA [92] for the separation of CO_2/H_2 mixtures in fixed-bed adsorbers using: (a) Ni-MOF-74 at CO_2 feed mole fractions of y_{CO_2} = 0.1, 0.2, 0.3, 0.4, 0.5, 0.9, (b) Cu-MOF-74 at CO_2 feed mole fractions of y_{CO_2} = 0.1, 0.2, 0.3, 0.4, 0.5, 0.9, (c) M-MOF-74, where M = Ni, Cu, Co, Fe, Mn, Zn at CO_2 feed mole fractions of y_{CO_2} = 0.5. The breakthrough curves of CO_2 are represented by dashed lines, and the breakthrough curves of H_2 by solid lines. The following dependencies are found: (1) the breakthrough time follows the same order as the uptake and the heat of CO_2 adsorption: Ni > Co > Fe > Mn > Zn > Cu, (2) the breakthrough time increases with decreasing mole fraction of CO_2 in the mixture. The initial conditions are specified as: temperature T = 298 K, total pressure p_T = 2.5 MPa, packed bed void fraction ϵ_B = 0.4, interstitial gas velocity entering the packed bed v = 0.006791 m s^{-1}, length of packed bed adsorber L = 0.065 m, axial dispersion is neglected, and isothermal conditions are assumed.

ethylenediamine, successfully applied to Mg-MOF-74 in the study of Wang et al. [103] The separation performance of the studied Mg-MOF-74 membrane was found to be improved, increasing the CO_2/H_2 selectivity from 10.5 to 28 due to the enhanced adsorption of CO_2 molecules by amine groups, thereby reducing the permeance of CO_2. Further studies of Ni-MOF-74 towards its application in separation processes may be a promising subject of research in the field of CO_2 and H_2 capture.

4. Conclusions

We carried out Monte Carlo simulations to adjust the non-polarizable force fields for CO_2 and H_2 adsorption in M-MOF-74, where M = Ni, Cu, Co, Fe, Mn, Zn. The model of CO_2 by Harris and Yung with LJ interactions parameters modeled by García-Sánchez et al. [72,73] was used in this study together with the three-site charge-quadrupole model of H_2 by Darkrim and Levesque [71]. LJ parameters from the DREIDING force field were used for the atoms of the frameworks, except for metal centers, which are defined by the UFF force field. We introduced two modifications to the existing force field for CO_2, H_2, and M-MOF-74: scaling the Coulombic interaction potentials of the framework atoms of M-MOF-74, and scaling LJ interaction potentials between the center of mass of H_2 and the open-metal centers. The force field was successfully validated by reproducing experimental CO_2 and H_2 isotherms, enthalpies of adsorption, binding geometries, and showing temperature transferability of the force field from 77 K to 87 K, and 298 K. The results agree well with the experimental measurements. The Feynman–Hibbs quantum correction was found to be an important part of the force field at cryogenic temperatures, as it affects the shape of the isotherm by reducing the adsorption capacity. The two-step mechanism of adsorption was recreated, wherein adsorbate molecules first adsorb at the metal centers, followed by adsorption above a triangle of oxygen atoms within the framework. The simulated uptake and heat of adsorption for CO_2 and H_2 reproduced the tendency in performance of M-MOF-74 from the experimental data. A small deviation was observed for the adsorption of H_2 in Fe-MOF-74, however the binding distance between H_2 and the metal center was reproduced most precisely for this MOF as 2.522 Å, deviating only by 0.3% from the literature value. The force field was applied to the adsorption of CO_2/H_2 mixtures at 298.15 K, and the prediction of breakthrough curves at 298 K. It was shown that almost no adsorption of H_2 occurs when CO_2 is present in the mixture. The breakthrough time follows the same order as the uptake and the heat of CO_2 adsorption: Ni > Co > Fe > Mn > Zn > Cu. The metal–organic frameworks M-MOF-74 have the potential in the capture of CO_2 and H_2, as well as in separation processes of CO_2/H_2 mixtures. The proposed non-polarizable force field is an alternative to the complex polarizable force fields available in the literature, that enables to fully investigate the performance of M-MOF-74 by molecular simulations. An interesting topic for future research would be the modification of the HCOOH force field to reproduce its binding geometry in M-MOF-74 obtained from DFT, to enable the application together with CO_2 and H_2 force fields. This would allow to study the process of CO_2 conversion into HCOOH,

and better understanding of the effect of open-metal centers on the CO_2 hydrogenation reaction to HCOOH in confinement.

CRediT authorship contribution statement

Dominika O. Wasik: Writing – review & editing, Writing – original draft, Visualization, Validation, Resources, Methodology, Investigation, Formal analysis, Data curation, Conceptualization. **José Manuel Vicent-Luna:** Software, Resources, Methodology, Conceptualization. **Azahara Luna-Triguero:** Resources, Investigation, Data curation, Conceptualization. **David Dubbeldam:** Software, Methodology. **Thijs J.H. Vlugt:** Writing – review & editing, Supervision. **Sofía Calero:** Supervision, Resources, Project administration, Funding acquisition, Conceptualization.

Declaration of competing interest

The authors declare that they have no known competing financial interests or personal relationships that could have appeared to influence the work reported in this paper.

Data availability

Data will be made available on request.

Acknowledgments

This research has been supported by the Eindhoven Institute for Renewable Energy Systems (EIRES).

Appendix A. Supplementary data

Supplementary material related to this article can be found online at https://doi.org/10.1016/j.seppur.2024.126539.

References

[1] X. Zhang, Z. Chen, X. Liu, S.L. Hanna, X. Wang, R. Taheri-Ledari, A. Maleki, P. Li, O.K. Farha, A historical overview of the activation and porosity of metal-organic frameworks, Chem. Soc. Rev. 49 (2020) 7406–7427.
[2] N.L. Rosi, J. Eckert, M. Eddaoudi, D.T. Vodak, J. Kim, M. O'Keeffe, O.M. Yaghi, Hydrogen storage in microporous metal-organic frameworks, Science 300 (5622) (2003) 1127–1129.
[3] M. Eddaoudi, J. Kim, N. Rosi, D. Vodak, J. Wachter, M. O'Keeffe, O.M. Yaghi, Systematic design of pore size and functionality in isoreticular MOFs and their application in methane storage, Science 295 (5554) (2002) 469–472.
[4] G. Férey, C. Mellot-Draznieks, C. Serre, F. Millange, J. Dutour, S. Surblé, I. Margiolaki, A chromium terephthalate-based solid with unusually large pore volumes and surface area, Science 309 (5743) (2005) 2040–2042.
[5] J.-R. Li, J. Sculley, H.-C. Zhou, Metal–organic frameworks for separations, Chem. Rev. 112 (2) (2012) 869–932.
[6] F.X. Llabrés i Xamena, A. Abad, A. Corma, H. Garcia, MOFs as catalysts: Activity, reusability and shape-selectivity of a Pd-containing MOF, J. Catal. 250 (2) (2007) 294–298.
[7] L. Alaerts, E. Séguin, H. Poelman, F. Thibault-Starzyk, P.A. Jacobs, D.E.D. Vos, Probing the lewis acidity and catalytic activity of the metal–organic framework $[Cu_3(btc)_2]$ (BTC = benzene-1,3,5-tricarboxylate), Chem. Eur. J. 12 (28) (2006) 7353–7363.
[8] Y. Chen, P. Li, J.A. Modica, R.J. Drout, O.K. Farha, Acid-resistant mesoporous metal–organic framework toward oral insulin delivery: Protein encapsulation, protection, and release, J. Am. Chem. Soc. 140 (17) (2018) 5678–5681.
[9] M.-X. Wu, Y.-W. Yang, Metal–organic framework (MOF)-based drug/cargo delivery and cancer therapy, Adv. Mater. 29 (23) (2017) 1606134.
[10] Y. Chen, P. Li, H. Noh, C.-W. Kung, C.T. Buru, X. Wang, X. Zhang, O.K. Farha, Stabilization of formate dehydrogenase in a metal–organic framework for bioelectrocatalytic reduction of CO_2, Angew. Chem. Int. Ed. 58 (23) (2019) 7682–7686.
[11] X. Lian, Y. Fang, E. Joseph, Q. Wang, J. Li, S. Banerjee, C. Lollar, X. Wang, H.-C. Zhou, Enzyme–MOF (metal–organic framework) composites, Chem. Soc. Rev. 46 (11) (2017) 3386–3401.
[12] B. Chen, Y. Yang, F. Zapata, G. Lin, G. Qian, E.B. Lobkovsky, Luminescent open metal sites within a metal–organic framework for sensing small molecules, Adv. Mater. 19 (13) (2007) 1693–1696.
[13] L.E. Kreno, K. Leong, O.K. Farha, M. Allendorf, R.P. Van Duyne, J.T. Hupp, Metal–organic framework materials as chemical sensors, Chem. Rev. 112 (2) (2012) 1105–1125.
[14] Q. Gu, H.Y. Ng, D. Zhao, J. Wang, Metal–organic frameworks (MOFs)-boosted filtration membrane technology for water sustainability, APL Mater. 8 (4) (2020) 040902.
[15] H.R. Abid, H. Tian, H.-M. Ang, M.O. Tade, C.E. Buckley, S. Wang, Nanosize Zr-metal organic framework (UiO-66) for hydrogen and carbon dioxide storage, Chem. Eng. J. 187 (2012) 415–420.
[16] H. Furukawa, K.E. Cordova, M. O'Keeffe, O.M. Yaghi, The chemistry and applications of metal-organic frameworks, Science 341 (6149) (2013) 1230444.
[17] P.D.C. Dietzel, B. Panella, M. Hirscher, R. Blom, H. Fjellvåg, Hydrogen adsorption in a nickel based coordination polymer with open metal sites in the cylindrical cavities of the desolvated framework, Chem. Commun. 9 (2006) 959–961.
[18] R. Sanz, F. Martínez, G. Orcajo, L. Wojtas, D. Briones, Synthesis of a honeycomb-like Cu-based metal–organic framework and its carbon dioxide adsorption behaviour, Dalton Trans. 42 (2013) 2392–2398.
[19] P.D. Dietzel, Y. Morita, R. Blom, H. Fjellvåg, An in situ high-temperature single-crystal investigation of a dehydrated metal–organic framework compound and field-induced magnetization of one-dimensional metal–oxygen chains, Angew. Chem. 117 (39) (2005) 6512–6516.
[20] S. Bhattacharjee, J.-S. Choi, S.-T. Yang, S.B. Choi, J. Kim, W.-S. Ahn, Solvothermal synthesis of Fe-MOF-74 and its catalytic properties in phenol hydroxylation, J. Nanosci. Nanotechnol. 10 (1) (2010) 135–141.
[21] W. Zhou, H. Wu, T. Yildirim, Enhanced H_2 adsorption in isostructural metal–organic frameworks with open metal sites: Strong dependence of the binding strength on metal ions, J. Am. Chem. Soc. 130 (46) (2008) 15268–15269.
[22] N.L. Rosi, J. Kim, M. Eddaoudi, B. Chen, M. O'Keeffe, O.M. Yaghi, Rod packings and metal-organic frameworks constructed from rod-shaped secondary building units, J. Am. Chem. Soc. 127 (5) (2005) 1504–1518.
[23] T. Pham, K.A. Forrest, R. Banerjee, G. Orcajo, J. Eckert, B. Space, Understanding the H_2 sorption trends in the M-MOF-74 series (M = Mg, Ni, Co, Zn), J. Phys. Chem. C 119 (2) (2015) 1078–1090.
[24] P. Dietzel, R. Johnsen, R. Blom, H. Fjellvåg, Structural changes and coordinatively unsaturated metal atoms on dehydration of honeycomb analogous microporous metal–organic frameworks, Chem. Eur. J. 14 (8) (2008) 2389–2397.
[25] J.L.C. Rowsell, O.M. Yaghi, Effects of functionalization, catenation, and variation of the metal oxide and organic linking units on the low-pressure hydrogen adsorption properties of metal–organic frameworks, J. Am. Chem. Soc. 128 (4) (2006) 1304–1315.
[26] W.L. Queen, M.R. Hudson, E.D. Bloch, J.A. Mason, M.I. Gonzalez, J.S. Lee, D. Gygi, J.D. Howe, K. Lee, T.A. Darwish, et al., Comprehensive study of carbon dioxide adsorption in the metal–organic frameworks M_2 (dobdc)(M = Mg, Mn, Fe, Co, Ni, Cu, Zn), Chem. Sci. 5 (12) (2014) 4569–4581.
[27] E.D. Bloch, W.L. Queen, R. Krishna, J.M. Zadrozny, C.M. Brown, J.R. Long, Hydrocarbon separations in a metal-organic framework with open iron(II) coordination sites, Science 335 (6076) (2012) 1606–1610.
[28] Y. Liu, H. Kabbour, C.M. Brown, D.A. Neumann, C.C. Ahn, Increasing the density of adsorbed hydrogen with coordinatively unsaturated metal centers in metal-organic frameworks, Langmuir 24 (9) (2008) 4772–4777.
[29] E.D. Bloch, L.J. Murray, W.L. Queen, S. Chavan, S.N. Maximoff, J.P. Bigi, R. Krishna, V.K. Peterson, F. Grandjean, G.J. Long, B. Smit, S. Bordiga, C.M. Brown, J.R. Long, Selective binding of O_2 over N_2 in a redox–active metal–organic framework with open iron(II) coordination sites, J. Am. Chem. Soc. 133 (37) (2011) 14814–14822.
[30] S. Horike, M. Dincă, K. Tamaki, J.R. Long, Size-selective lewis acid catalysis in a microporous metal-organic framework with exposed Mn^{2+} coordination sites, J. Am. Chem. Soc. 130 (18) (2008) 5854–5855.
[31] H. Irving, R. Williams, Order of stability of metal complexes, Nature 162 (4123) (1948) 746–747.
[32] D. Yu, A.O. Yazaydin, J.R. Lane, P.D.C. Dietzel, R.Q. Snurr, A combined experimental and quantum chemical study of CO_2 adsorption in the metal–organic framework CPO-27 with different metals, Chem. Sci. 4 (2013) 3544–3556.
[33] D. Dubbeldam, S. Calero, T.J.H. Vlugt, iRASPA: GPU-accelerated visualization software for materials scientists, Mol. Simul. 44 (8) (2018) 653–676.
[34] European Commission Joint Research Centre (JRC)/Netherlands Environmental Assessment Agency (PBL), Emission database for global atmospheric research (EDGAR), 2023, http://edgar.jrc.ec.europa.eu; access date: 28 July 2023.
[35] M. Radosz, X. Hu, K. Krutkramelis, Y. Shen, Flue-gas carbon capture on carbonaceous sorbents: Toward a low-cost multifunctional carbon filter for "green" energy producers, Ind. Eng. Chem. Res. 47 (10) (2008) 3783–3794.
[36] J.S. Yeon, W.R. Lee, N.W. Kim, H. Jo, H. Lee, J.H. Song, K.S. Lim, D.W. Kang, J.G. Seo, D. Moon, B. Wiers, C.S. Hong, Homodiamine-functionalized metal–organic frameworks with a MOF-74-type extended structure for superior selectivity of CO_2 over N_2, J. Mater. Chem. A 3 (2015) 19177–19185.
[37] T. Zurrer, K. Wong, J. Horlyck, E.C. Lovell, J. Wright, N.M. Bedford, Z. Han, K. Liang, J. Scott, R. Amal, Mixed-metal MOF-74 templated catalysts for efficient carbon dioxide capture and methanation, Adv. Funct. Mater. 31 (9) (2021) 2007624.

[38] J.H. Choe, H. Kim, C.S. Hong, MOF-74 type variants for CO_2 capture, Mater. Chem. Front. 5 (2021) 5172–5185.

[39] W. Meng, Y. Zeng, Z. Liang, W. Guo, C. Zhi, Y. Wu, R. Zhong, C. Qu, R. Zou, Tuning expanded pores in metal–organic frameworks for selective capture and catalytic conversion of carbon dioxide, ChemSusChem 11 (21) (2018) 3751–3757.

[40] C. Chen, X. Feng, Q. Zhu, R. Dong, R. Yang, Y. Cheng, C. He, Microwave-assisted rapid synthesis of well-shaped MOF-74 (Ni) for CO_2 efficient capture, Inorg. Chem. 58 (4) (2019) 2717–2728.

[41] D.S. Newsome, The water-gas shift reaction, Catal. Rev. Sci. Eng. 21 (2) (1980) 275–318.

[42] Z. Qiao, N. Wang, J. Jiang, J. Zhou, Design of amine-functionalized metal–organic frameworks for CO_2 separation: the more amine, the better? Chem. Commun. 52 (2016) 974–977.

[43] D.M. Ruthven, S. Farooq, K.S. Knaebel, Pressure Swing Adsorption, John Wiley & Sons, 1996.

[44] G.T. Rochelle, Amine scrubbing for CO_2 capture, Science 325 (5948) (2009) 1652–1654.

[45] A. Iulianelli, C. Pirola, A. Comazzi, F. Galli, F. Manenti, A. Basile, 1 - water gas shift membrane reactors, in: A. Basile, L. Di Paola, F. I. Hai, V. Piemonte (Eds.), Membrane Reactors for Energy Applications and Basic Chemical Production, in: Woodhead Publishing Series in Energy, Woodhead Publishing, 2015, pp. 3–29.

[46] H. Hiller, R. Reimert, F. Marschner, H.-J. Renner, W. Boll, E. Supp, M. Brejc, W. Liebner, G. Schaub, G. Hochgesand, C. Higman, P. Kalteier, W.-D. Müller, M. Kriebel, H. Schlichting, H. Tanz, H.-M. Stönner, H. Klein, W. Hilsebein, V. Gronemann, U. Zwiefelhofer, J. Albrecht, C.J. Cowper, H.E. Driesen, Gas production, in: Ullmann's Encyclopedia of Industrial Chemistry, sixth ed., John Wiley & Sons, Ltd, 2006.

[47] Z.R. Herm, J.A. Swisher, B. Smit, R. Krishna, J.R. Long, Metal–organic frameworks as adsorbents for hydrogen purification and precombustion carbon dioxide capture, J. Am. Chem. Soc. 133 (15) (2011) 5664–5667.

[48] G.O. Aksu, H. Daglar, C. Altintas, S. Keskin, Computational selection of high-performing covalent organic frameworks for adsorption and membrane-based CO_2/H_2 separation, J. Phys. Chem. C 124 (41) (2020) 22577–22590.

[49] P.D.C. Dietzel, P.A. Georgiev, J. Eckert, R. Blom, T. Strässle, T. Unruh, Interaction of hydrogen with accessible metal sites in the metal-organic frameworks M_2 (dhtp) (CPO-27-M; M = Ni, Co, Mg), Chem. Commun. 46 (2010) 4962–4964.

[50] C.M. Brown, A.J. Ramirez-Cuesta, J.-H. Her, P.S. Wheatley, R.E. Morris, Structure and spectroscopy of hydrogen adsorbed in a nickel metal–organic framework, Chem. Phys. 427 (2013) 3–8.

[51] M.H. Rosnes, M. Opitz, M. Frontzek, W. Lohstroh, J.P. Embs, P.A. Georgiev, P.D. Dietzel, Intriguing differences in hydrogen adsorption in CPO-27 materials induced by metal substitution, J. Mater. Chem. A 3 (9) (2015) 4827–4839.

[52] A.G. Wong-Foy, A.J. Matzger, O.M. Yaghi, Exceptional H_2 saturation uptake in microporous metal-organic frameworks, J. Am. Chem. Soc. 128 (11) (2006) 3494–3495.

[53] M.T. Kapelewski, S.J. Geier, M.R. Hudson, D. Stück, J.A. Mason, J.N. Nelson, D.J. Xiao, Z. Hulvey, E. Gilmour, S.A. FitzGerald, M. Head-Gordon, C.M. Brown, J.R. Long, M_2(m-dobdc) (M = Mg, Mn, Fe, Co, Ni) metal–organic frameworks exhibiting increased charge density and enhanced H_2 binding at the open metal sites, J. Am. Chem. Soc. 136 (34) (2014) 12119–12129.

[54] M. Märcz, R.E. Johnsen, P.D. Dietzel, H. Fjellvåg, The iron member of the CPO-27 coordination polymer series: Synthesis, characterization, and intriguing redox properties, Microporous Mesop. Mater. 157 (2012) 62–74.

[55] W.L. Queen, E.D. Bloch, C.M. Brown, M.R. Hudson, J.A. Mason, L.J. Murray, A.J. Ramirez-Cuesta, V.K. Peterson, J.R. Long, Hydrogen adsorption in the metal–organic frameworks Fe_2(dobdc) and $Fe_2(O_2)$(dobdc), Dalton Trans. 41 (2012) 4180–4187.

[56] S.C. Peter, Reduction of CO_2 to chemicals and fuels: A solution to global warming and energy crisis, ACS Energy Lett. 3 (2018) 1557–1561.

[57] N.M. Dowell, P.S. Fennell, N. Shah, G.C. Maitland, The role of CO_2 capture and utilization in mitigating climate change, Nature Clim. Change 7 (2017) 243–249.

[58] N.B. Singh, in: H. Pöllmann (Ed.), In Conversion of CO_2 Into Useful Products. Industrial Waste: Characterization, Modification and Applications of Residues, fourth ed., De Gruyter, Berlin, Boston, 2021, pp. 319–344.

[59] M. Aresta (Ed.), Carbon Dioxide Recovery and Utilization, fourth ed., Kluwer Academic Publishers, Dordrecht, 2010.

[60] D.O. Wasik, A. Martín-Calvo, J.J. Gutiérrez-Sevillano, D. Dubbeldam, T.J.H. Vlugt, S. Calero, Enhancement of formic acid production from carbon dioxide hydrogenation using metal-organic frameworks: Monte Carlo simulation study, Chem. Eng. J. 467 (2023) 143432.

[61] S. Moret, P.J. Dyson, G. Laurenczy, Direct synthesis of formic acid from carbon dioxide by hydrogenation in acidic media, Nature Commun. 5 (2014) 4017.

[62] M. Ghara, P.K. Chattaraj, A computational study on hydrogenation of CO_2, catalyzed by a bridged B/N frustrated lewis pair, Struct. Chem. 30 (2019) 1067–1077.

[63] H. Le Chatelier, O. Boudouard, On the flammable limits of gas mixtures, Process Safety Prog. 24 (1) (2005) 3–5.

[64] T.M. Becker, D. Dubbeldam, L.-C. Lin, T.J.H. Vlugt, Investigating polarization effects of CO_2 adsorption in Mg-MOF-74, J. Comput. Sci. 15 (2016) 86–94.

[65] T.M. Becker, J. Heinen, D. Dubbeldam, L.-C. Lin, T.J.H. Vlugt, Polarizable force fields for CO_2 and CH_4 adsorption in M-MOF-74, J. Phys. Chem. C 121 (8) (2017) 4659–4673.

[66] T.M. Becker, L.-C. Lin, D. Dubbeldam, T.J.H. Vlugt, Polarizable force field for CO_2 in M-MOF-74 derived from quantum mechanics, J. Phys. Chem. C 122 (42) (2018) 24488–24498.

[67] R. Mercado, B. Vlaisavljevich, L.-C. Lin, K. Lee, Y. Lee, J.A. Mason, D.J. Xiao, M.I. Gonzalez, M.T. Kapelewski, J.B. Neaton, B. Smit, Force field development from periodic density functional theory calculations for gas separation applications using metal–organic frameworks, J. Phys. Chem. C 120 (23) (2016) 12590–12604.

[68] L.-C. Lin, K. Lee, L. Gagliardi, J.B. Neaton, B. Smit, Force-field development from electronic structure calculations with periodic boundary conditions: Applications to gaseous adsorption and transport in metal–organic frameworks, J. Chem. Theory Comput. 10 (4) (2014) 1477–1488.

[69] V. Buch, Path integral simulations of mixed *para*-D_2 and *ortho*-D_2 clusters: The orientational effects, J. Chem. Phys. 100 (10) (1994) 7610–7629.

[70] J.L. Belof, A.C. Stern, B. Space, An accurate and transferable intermolecular diatomic hydrogen potential for condensed phase simulation, J. Chem. Theory Comput. 4 (8) (2008) 1332–1337.

[71] F. Darkrim, D. Levesque, Monte Carlo simulations of hydrogen adsorption in single-walled carbon nanotubes, J. Chem. Phys. 109 (12) (1998) 4981–4984.

[72] J.G. Harris, K.H. Yung, Carbon dioxide's liquid-vapor coexistence curve and critical properties as predicted by a simple molecular model, J. Phys. Chem. 99 (31) (1995) 12021–12024.

[73] A. García-Sánchez, C.O. Ania, J.B. Parra, D. Dubbeldam, T.J.H. Vlugt, R. Krishna, S. Calero, Transferable force field for carbon dioxide adsorption in zeolites, J. Phys. Chem. C 113 (20) (2009) 8814–8820.

[74] F.J. Salas, E. Nunez-Rojas, J. Alejandre, Stability of formic acid/pyridine and isonicotinamide/formamide cocrystals by molecular dynamics simulations, Theor. Chem. Acc. 136 (1) (2017) 1–12.

[75] D.O. Wasik, H.M. Polat, M. Ramdin, O.A. Moultos, S. Calero, T.J.H. Vlugt, Solubility of CO_2 in aqueous formic acid solutions and the effect of NaCl addition: A molecular simulation study, J. Phys. Chem. C 126 (45) (2022) 19424–19434.

[76] M.P. Allen, D.J. Tildesley, Computer Simulation of Liquids, second ed., Oxford University Press, Oxford, UK, 2017.

[77] B.A. Wells, A.L. Chaffee, Ewald summation for molecular simulations, J. Chem. Theory Comput. 11 (8) (2015) 3684–3695.

[78] S.L. Mayo, B.D. Olafson, W.A. Goddard, DREIDING: a generic force field for molecular simulations, J. Phys. Chem. 94 (26) (1990) 8897–8909.

[79] A.K. Rappe, C.J. Casewit, K.S. Colwell, W.A. Goddard, W.M. Skiff, UFF, a full periodic table force field for molecular mechanics and molecular dynamics simulations, J. Am. Chem. Soc. 114 (25) (1992) 10024–10035.

[80] D. Dubbeldam, S. Calero, D.E. Ellis, R.Q. Snurr, RASPA: Molecular simulation software for adsorption and diffusion in flexible nanoporous materials, Mol. Simul. 42 (2) (2016) 81–101.

[81] D. Dubbeldam, A. Torres-Knoop, K.S. Walton, On the inner workings of Monte Carlo codes, Mol. Simul. 39 (14–15) (2013) 1253–1292.

[82] D. Frenkel, B. Smit, Understanding Molecular Simulation: From Algorithms to Applications, third ed., Elsevier, 2023.

[83] C.E. Wilmer, R.Q. Snurr, Towards rapid computational screening of metal-organic frameworks for carbon dioxide capture: Calculation of framework charges via charge equilibration, Chem. Eng. J. 171 (3) (2011) 775–781.

[84] C.E. Wilmer, K.C. Kim, R.Q. Snurr, An extended charge equilibration method, J. Phys. Chem. Lett. 3 (17) (2012) 2506–2511.

[85] P. Atkins, J. De Paula, J. Keeler, Atkins' Physical Chemistry, twelfth ed., Oxford University Press, 2023.

[86] R.P. Feynman, A.R. Hibbs, D.F. Styer, Quantum Mechanics and Path Integrals, Courier Corporation, 2010.

[87] S.K. Bhatia, A.L. Myers, Optimum conditions for adsorptive storage, Langmuir 22 (4) (2006) 1688–1700.

[88] K.S. Deeg, J.J. Gutiérrez-Sevillano, R. Bueno-Pérez, J.B. Parra, C.O. Ania, M. Doblaré, S. Calero, Insights on the molecular mechanisms of hydrogen adsorption in zeolites, J. Phys. Chem. C 117 (27) (2013) 14374–14380.

[89] A.V.A. Kumar, H. Jobic, S.K. Bhatia, Quantum effects on adsorption and diffusion of hydrogen and deuterium in microporous materials, J. Phys. Chem. B 110 (33) (2006) 16666–16671.

[90] A. Martin-Calvo, J.J. Gutiérrez-Sevillano, I. Matito-Martos, T.J.H. Vlugt, S. Calero, Identifying zeolite topologies for storage and release of hydrogen, J. Phys. Chem. C 122 (23) (2018) 12485–12493.

[91] J. Baker, An algorithm for the location of transition states, J. Comput. Chem. 7 (4) (1986) 385–395.

[92] S. Sharma, S.R.G. Balestra, R. Baur, U. Agarwal, E. Zuidema, M.S. Rigutto, S. Calero, T.J.H. Vlugt, D. Dubbeldam, RUPTURA: Simulation code for breakthrough, ideal adsorption solution theory computations, and fitting of isotherm models, Mol. Simul. 49 (9) (2023) 893–953.

[93] I. Langmuir, The adsorption of gases on plane surfaces of glass, mica and platinum, J. Am. Chem. Soc. 40 (9) (1918) 1361–1403.

[94] S.J. Caldwell, B. Al-Duri, N. Sun, C.-g. Sun, C.E. Snape, K. Li, J. Wood, Carbon dioxide separation from nitrogen/hydrogen mixtures over activated carbon beads: Adsorption isotherms and breakthrough studies, Energy Fuels 29 (6) (2015) 3796–3807.

[95] A.L. Myers, J.M. Prausnitz, Thermodynamics of mixed-gas adsorption, AIChE J. 11 (1) (1965) 121–127.

[96] A. Luna-Triguero, J.M. Vicent-Luna, R.M. Madero-Castro, P. Gómez-Álvarez, S. Calero, Acetylene storage and separation using metal–organic frameworks with open metal sites, ACS Appl. Mater. Interfaces 11 (34) (2019) 31499–31507.

[97] W. Li, C.Y. Chuah, Y. Yang, T.-H. Bae, Nanocomposites formed by in situ growth of NiDOBDC nanoparticles on graphene oxide sheets for enhanced CO_2 and h_2 storage, Microporous Mesop. Mater. 265 (2018) 35–42.

[98] P.D.C. Dietzel, R.E. Johnsen, H. Fjellvåg, S. Bordiga, E. Groppo, S. Chavan, R. Blom, Adsorption properties and structure of CO_2 adsorbed on open coordination sites of metal–organic framework Ni_2(dhtp) from gas adsorption, IR spectroscopy and X-ray diffraction, Chem. Commun. (2008) 5125–5127.

[99] Y. Chen, S. Li, X. Pei, J. Zhou, X. Feng, S. Zhang, Y. Cheng, H. Li, R. Han, B. Wang, A solvent-free hot-pressing method for preparing metal–organic-framework coatings, Angew. Chem. Int. Ed. 55 (10) (2016) 3419–3423.

[100] D.-L. Chen, H. Shang, W. Zhu, R. Krishna, Transient breakthroughs of CO_2/CH_4 and C_3H_6/C_3H_8 mixtures in fixed beds packed with Ni-MOF-74, Chem. Eng. Sci. 117 (2014) 407–415.

[101] S. Pu, J. Wang, L. Li, Z. Zhang, Z. Bao, Q. Yang, Y. Yang, H. Xing, Q. Ren, Performance comparison of metal–organic framework extrudates and commercial zeolite for ethylene/ethane separation, Ind. Eng. Chem. Res. 57 (5) (2018) 1645–1654.

[102] Q. Al-Naddaf, H. Thakkar, F. Rezaei, Novel zeolite-5A@MOF-74 composite adsorbents with core–shell structure for H_2 purification, ACS Appl. Mater. Interfaces 10 (35) (2018) 29656–29666.

[103] N. Wang, A. Mundstock, Y. Liu, A. Huang, J. Caro, Amine-modified Mg-MOF-74/CPO-27-Mg membrane with enhanced H_2/CO_2 separation, Chem. Eng. Sci. 124 (2015) 27–36.